Contributions to Mineralogy and Petrology (2024) 179:46
https://doi.org/10.1007/s00410-024-02117-0

ORIGINAL PAPER

Testing in-situ apatite Lu–Hf dating in polymetamorphic mafic rocks: a case study from Palaeoproterozoic southern Australia

Dillon A. Brown[1,2] · Anthony Reid[1,2] · Elizabeth A. Jagodzinski[1] · Megan Williams[1] · Alex Simpson[2] · Mark Pawley[1] · Christopher L. Kirkland[3] · Claire Wade[1,2] · Alexander T. De Vries Van Leeuwen[1,2,4] · Stijn Glorie[2]

Received: 30 October 2023 / Accepted: 6 March 2024 / Published online: 15 April 2024

Abstract

In mafic systems where primary mineral assemblages have witnessed moderate- to high-temperature hydrous overprinting and deformation, little is known about the retentivity of the Lu–Hf isotopic system in apatite. This study presents apatite laser-ablation Lu–Hf and U–Pb geochronology, zircon geochronology, and detailed petrological information from polymetamorphic mafic intrusions located in the central-western Gawler Craton in southern Australia, which records an extensive tectonometamorphic history spanning the Neoarchaean to the Mesoproterozoic. Zircon records magmatic crystallisation ages of c. 2479–2467 Ma, coinciding with the onset of the c. 2475–2410 Ma granulite-facies Sleafordian Orogeny. The amphibole-dominant hydrous assemblages which extensively overprint the primary magmatic assemblages are hypothesised to post-date the Sleafordian Orogeny. The Lu–Hf and U–Pb isotopic systems in apatite are used to test this hypothesis, with both isotopic systems recording significantly younger ages correlating with the c. 1730–1690 Ma Kimban Orogeny and the c. 1590–1575 Ma Hiltaba magmatic event, respectively. While the early Mesoproterozoic apatite U–Pb ages are attributed to thermal re-equilibration, the older Lu–Hf ages are interpreted to reflect re-equilibration facilitated primarily by dissolution-reprecipitation, but also thermally activated volume diffusion. The mechanisms of Lu–Hf isotopic resetting are distinguished based on microscale textures and trace element abundances in apatite and the integration of apatite-amphibole textural relationships and temperatures determined from the Ti content in amphibole. More broadly, the results indicate that at low to moderate temperatures, apatite hosted in mafic rocks is susceptible to complete recrystallisation in rocks that have weak to moderate foliations. In contrast, at higher temperatures in the absence of strain, the Lu–Hf system in apatite is comparatively robust. Ultimately, the findings from this study advance our understanding of the complex role that both metamorphism and deformation play on the ability of mafic-hosted apatite to retain primary Lu–Hf isotopic signatures.

Keywords Geochronology · Apatite · Lu–Hf · Isotopic resetting · Mafic rocks · Polymetamorphism

Introduction

Investigations of the interaction between the mantle and crust through time requires the application of robust geochronological techniques to mafic rocks (e.g., Dai et al. 2011; Orejana et al. 2020; Wade et al. 2022). However, relative to felsic igneous rocks, metamorphic rocks, and metasedimentary rocks, mafic rocks are typically difficult to date due to the scarcity of minerals such as zircon or baddeleyite. An alternative mineral amenable to geochronology is apatite, which is a common accessory mineral in a range of rock types, including mafic and ultramafic lithologies (e.g., Pochon et al. 2016; Gillespie et al. 2018; Henrichs et al. 2018; Kirkland et al. 2018; O'Sullivan et al. 2020; Nixon et al. 2022; Cave et al. 2023; Kharkongor et al. 2023). The

Communicated by Dante Canil.

✉ Dillon A. Brown
dillon.brown@sa.gov.au

[1] Department for Energy and Mining, Geological Survey of South Australia, Adelaide, SA, Australia

[2] Department of Earth Sciences, University of Adelaide, Adelaide, SA, Australia

[3] Timescales of Mineral Systems Group, School of Earth and Planetary Sciences, Curtin University, Perth, WA, Australia

[4] Mineral Exploration Cooperative Research Centre, Kensington, WA, Australia

U–Pb system in apatite has been primarily used to constrain the timing of low- to moderate-temperature metamorphic and metasomatic processes (e.g., Kirkland et al. 2017, 2018; Hall et al. 2018; Henrichs et al. 2018; Glorie et al. 2019), with estimates for the U–Pb closure temperature from 375 to 550 °C (Schoene and Bowring 2007; Chew et al. 2011; Cochrane et al. 2014). However, recent advances utilising the Lu–Hf isotopic system have demonstrated the potential of apatite to date magmatic and higher temperature metamorphic processes (e.g., Barfod et al. 2005; Simpson et al. 2021; Gillespie et al. 2022; Glorie et al. 2022, 2023).

It is not uncommon for the Lu–Hf system in apatite to record older ages compared to the U–Pb system (e.g., Gillespie et al. 2022; Glorie et al. 2023; Kharkongor et al. 2023), with estimates for the Lu–Hf closure temperature between 660 and 730 °C (Cherniak 2000; Barfod et al. 2005; Chew and Spikings 2015; Glorie et al. 2023). Lu–Hf dates recovered from predominantly undeformed granitoids are in general agreement with primary crystallisation ages obtained from magmatic and high-temperature metamorphic geochronometers such as zircon (e.g., Simpson et al. 2021; Gillespie et al. 2022; Glorie et al. 2023). However, apatite is more susceptible to recrystallisation during deformation, and it has been shown that in-situ Lu–Hf dates from apatite in deformed rocks tend to reflect recrystallisation instead of primary magmatic crystallisation (Glorie et al. 2023). Furthermore, when the sampled rocks have experienced upper amphibolite- to granulite-facies conditions, it has been demonstrated that Hf retentivity can be compromised, leading to either metamorphic or cooling ages. In the context of mafic–ultramafic rocks, Kharkongor et al. (2023) has recently shown that apatite Lu–Hf dates generally reflect the timing of emplacement in rocks that are relatively undeformed and lack high-temperature mineralogical overprints. Despite these recent insights into the Lu–Hf systematics in apatite, the behaviour of this isotopic system in apatite is not yet well understood in the context of deformed rocks that have witnessed multiple metamorphic and/or metasomatic events.

This study aims to explore the response of the Lu–Hf system in apatite to multiple metamorphic events of varying intensity which were imposed on mafic intrusions from the central-western Gawler Craton in southern Australia (Fig. 1). The tectonometamorphic history of the Gawler Craton is extensive and spans the Mesoarchaean to the Mesoproterozoic, with the central-western region of the craton preserving Neoarchaean to early Palaeoproterozoic basement intruded and overlain by Palaeo- to Mesoproterozoic granitoids, volcanics, and sedimentary sequences (Hand et al. 2007; Reid and Hand 2012). In this study, the apatite Lu–Hf geochronometer is compared to the U–Pb geochronometer in both apatite and zircon, with the comparison between the zircon U–Pb and apatite Lu–Hf systems affording an opportunity to evaluate the factors contributing to Hf re-equilibration in apatite from mineralogically complex polymetamorphic mafic rocks. We use trace and rare earth element compositions to establish whether apatite is primary magmatic or has recrystallised, with recent studies demonstrating the potential of apatite to fingerprint source characteristics (e.g., Henrichs et al. 2018; O'Sullivan et al. 2020). Additionally, a detailed petrological study is undertaken on the mafic intrusions and the textural relationships between apatite and the primary mineral phases in each sample are explored, particularly the relationships between apatite and amphibole. Finally, titanium in amphibole thermometry targeting different textural generations of amphibole (including those in textural equilibrium with apatite) is implemented to provide supporting evidence in the assessment of whether thermal volume diffusion is sufficient to explain patterns of Lu–Hf isotopic disturbance in apatite.

Geological background

Mulgathing Complex, southern Australia

The Archaean to early Palaeoproterozoic Mulgathing Complex of the central-western Gawler Craton in southern Australia is a diverse lithostratigraphic package containing variably deformed metasedimentary and meta-igneous rocks, and felsic to mafic intrusive and volcaniclastic rocks (Fig. 1; Jagodzinski et al. 2009; Reid et al. 2014; Williams and Reid 2021). A detailed summary of the stratigraphic units is provided by Reid et al. (2014). The lithologies of the Mulgathing Complex preserve a c. 2558–2467 Ma record of contractional and extensional tectonics, basin development, and punctuated bimodal magmatism (Swain et al. 2005; Fanning et al. 2007; Reid et al. 2014). Sedimentation and punctuated mantle-derived magmatism occurred within a back-arc setting, while basin inversion and crustal shortening from c. 2470 Ma to c. 2410 Ma during the Sleafordian Orogeny resulted in an amphibolite- to granulite-facies overprint on the sedimentary and igneous protoliths, with the orogenic episode characterised by prolonged high thermal gradients, anatexis, and erosion-driven exhumation (McFarlane 2006; Reid et al. 2014; Halpin and Reid 2016). Peak metamorphic conditions for the Sleafordian Orogeny in the central Gawler Craton are constrained to ~ 7 kbar and ~ 850 °C at c. 2470 Ma (Halpin and Reid 2016). In the equivalent rocks of the Sleaford Complex in the southern Gawler Craton, pressures and temperatures have been estimated at 4.5–6 kbar and 750–780 °C (Dutch et al. 2010).

The Mulgathing Complex is interpreted to form the basement to Palaeo- to Mesoproterozoic units occurring in the Christie, Wilgena, and Harris Greenstone domains of the Gawler Craton (Figs. 1, 2). Granitoid suites intruding

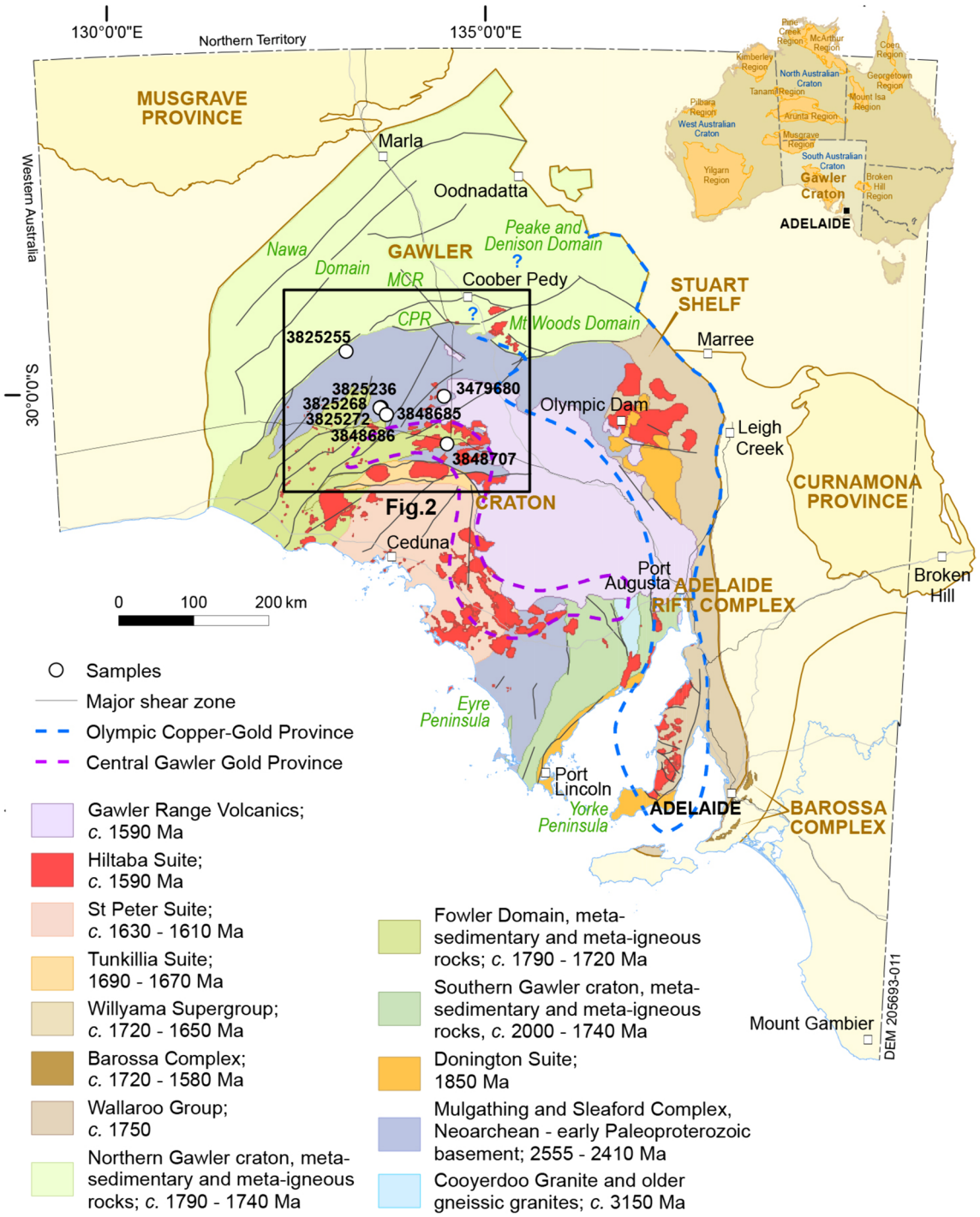

Fig. 1 Simplified map of the Gawler Craton solid geology showing the locations of samples investigated in this study. Map sourced from the Department for Energy and Mining, South Australia

the Mulgathing Complex include the c. 1745–1700 Ma Peter Pan Supersuite (Wade and McAvaney 2017), the c. 1690–1670 Ma Tunkillia Suite (Ferris and Schwarz 2004; Payne et al. 2010), and the c. 1590–1575 Ma Hiltaba Suite (Budd 2006; Bockmann et al. 2019; Reid et al. 2021). Granitoids of the Peter Pan Supersuite were emplaced prior to and during the c. 1730–1690 Ma Kimban Orogeny (Parker 1993), while the felsic Tunkillia Suite is post-tectonic relative to the Kimban Orogeny (Payne et al. 2010). This major Gawler Craton-wide tectonometamorphic event reworked older Archean to Palaeoproterozoic basement and cover sequences, with its expression most obvious in the

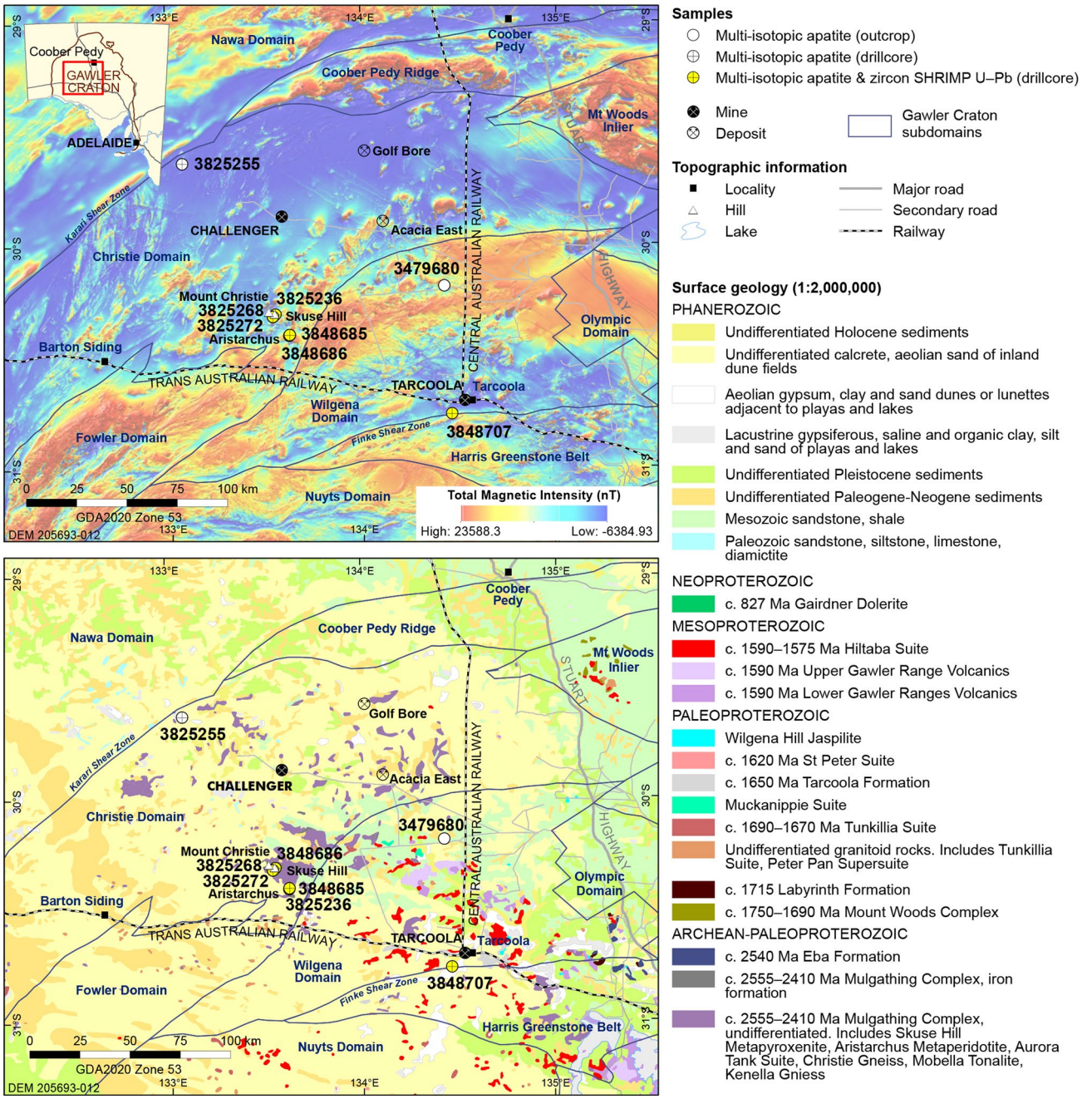

Fig. 2 Total Magnetitic Intensity (TMI) and surface geology maps (1:2 000 000) of the central-western Gawler Craton region, with the locations of investigated samples. Provided are the Gawler Craton domains and boundaries as referred to in the text. Inset shows the extent of the Gawler Craton with reference to South Australia. Base maps sourced from the Department for Energy and Mining, South Australia

southern Gawler Craton (Fig. 1), where granulite-facies mineral assemblages developed at conditions of 8–9 kbar and 820–850 °C (Dutch et al. 2010; Hand et al. 2012). However, the metamorphic and petrological character of this Kimban-aged overprint is poorly understood in the equivalent early Palaeoproterozoic rocks of the Mulgathing Complex to the north.

Mafic magmatism and sedimentation, Mulgathing Complex

The c. 2520 Ma Harris Greenstone Belt of the Gawler Craton comprises compositionally depleted mafic and ultramafic volcanic rocks interbedded with metasedimentary and volcaniclastic rocks (Hoatson et al. 2005; Swain et al. 2005).

Associated with the Harris Greenstone Belt is the metasedimentary Christie Gneiss, which contains variable lithologies with maximum depositional ages of c. 2520 Ma, c. 2515 Ma, and c. 2480 Ma (Swain et al. 2005; McFarlane et al. 2007; Jagodzinski et al. 2009; Reid et al. 2014). A series of early Palaeoproterozoic mafic and felsic rocks intrude the Christie Gneiss. At the Aristarchus prospect in the southern Christie Domain, the Burden Metagabbro gives a crystallisation age of c. 2488 Ma (Reid et al. 2014). Other gabbroic lithologies at the Aristarchus prospect (termed the Aristarchus Metaperidotite) are also interpreted to intrude the Christie Gneiss, but are hypothesised to be younger than c. 2475 Ma based on their association with c. 2475–2470 Ma granitic gneiss of the Aurora Tank Suite (Williams and Reid 2021), which is interpreted to intrude both the Christie Gneiss and Burden Metagabbro (Jagodzinski et al. 2009; Reid et al. 2014; Jagodzinski and Reid 2017; Williams and Reid 2021). The youngest mafic units of the Mulgathing Complex are dated at c. 2461 Ma and occur in the Skuse Hill region near Mount Christie (Fig. 2). These gabbroic lithologies intrude the Christie Gneiss and are part of the Skuse Hill Metapyroxenite (Fanning et al. 2007; Williams and Reid 2021).

Samples

Mafic units hypothesised to have been emplaced pre- and syn-Sleafordian Orogeny were sampled from across the central-western Gawler Craton (Figs. 1, 2). Samples were collected from both outcrop and drill core. Drill core samples were obtained from the South Australia Drill Core Reference Library, located in Tonsley, South Australia. Sample details and mineral assemblages are given in Table 1, with locations shown in Fig. 2. The following brief sample descriptions emphasise the textural relationships between in-situ apatite and different textural generations of amphibole, given the samples typically contain amphibole-dominant overprints and compositional data has been collected from both apatite and amphibole in this study. The amphibole textural generations (abbreviated amp^1, amp^2, amp^3; Fig. 3) are sample-specific. Detailed individual sample descriptions, including a comprehensive set of drill core images and photomicrographs, are provided in supplementary material 1 (Figs. S1–S4). A summary of the apatite and zircon geochronological results from this study are provided in Table 2.

Muckanippie region

Sample 3479680 is from an outcrop of the Muckanippie Suite in the northern Wilgena Domain of the central Gawler Craton (Fig. 2; Table 1). The sample is an unfoliated medium- to coarse-grained equigranular anorthosite, containing primarily plagioclase, amphibole, and orthopyroxene (Figs. S1–S4). Subhedral to anhedral dark green to brown amphibole (amp^1) is typically preserved as medium- to coarse-grained masses and almost completely overprints relict medium-grained orthopyroxene. Green–brown amphibole is partially replaced by a second generation of blue-green

Table 1 Sample information

Sample	Drillhole	Stratigraphic unit	Interval (m)	Lat, Long	Lithology	Assemblage	Texture
3479680	–	Muckanippie Anorthosite	–	−30.19339, 134.42589	Anorthosite	pl-amp-opx-mag ± bt-hem-chl-ep-ap	Unfoliated
3825236	SKUSE HILL 2	Skuse Hill Metapyroxenite	70.39–71.54	−30.31889, 133.55097	Metapyroxenite	opx-cpx-bt-pl ± mnz-ap-py/ccp	Moderately foliated
3825255	NNL IL2 DDH 1	Mobella Tonalite	114.30–115.38	−29.63720, 133.07996	Amp metanorite	amp-pl-bt-opx-mag ± ilm-ap	Unfoliated
3825268	BLACKFELLOW HILL 1	Skuse Hill Metapyroxenite	90.19–91.83	−30.32885, 133.53766	Bt amphibolite	amp-bt ± ap-ilm-py/ccp	Weakly foliated
3825272	BLACKFELLOW HILL 1	Skuse Hill Metapyroxenite	143.07–143.80	−30.32885, 133.53766	Pl-bt amphibolite	amp-pl-bt-ilm ± py/ccp-ap-aln-mnz	Weakly foliated
3848685	DMDD-001	Aristarchus Metaperidotite	193.00–194.43	−30.41104, 133.62248	Amp metagabbro	pl-cpx-amp-ilm ± bt-chl-mag-ap-py/ccp	Weakly foliated
3848686	DMDD-001	Aristarchus Metaperidotite	214.43–216.08	−30.41104, 133.62248	Bt amphibolite	amp-bt-cpx ± ilm-mag-ap-py/ccp	Moderately foliated
3848707	BGDDH 4	Unassigned	109.92–110.70	−30.76781, 134.46395	Amp-bt diorite	amp-pl-bt ± ccp-ap-mag-ilm-chl-ep-mnz	Weakly foliated

Mineral abbreviations after Whitney and Evans (2010)

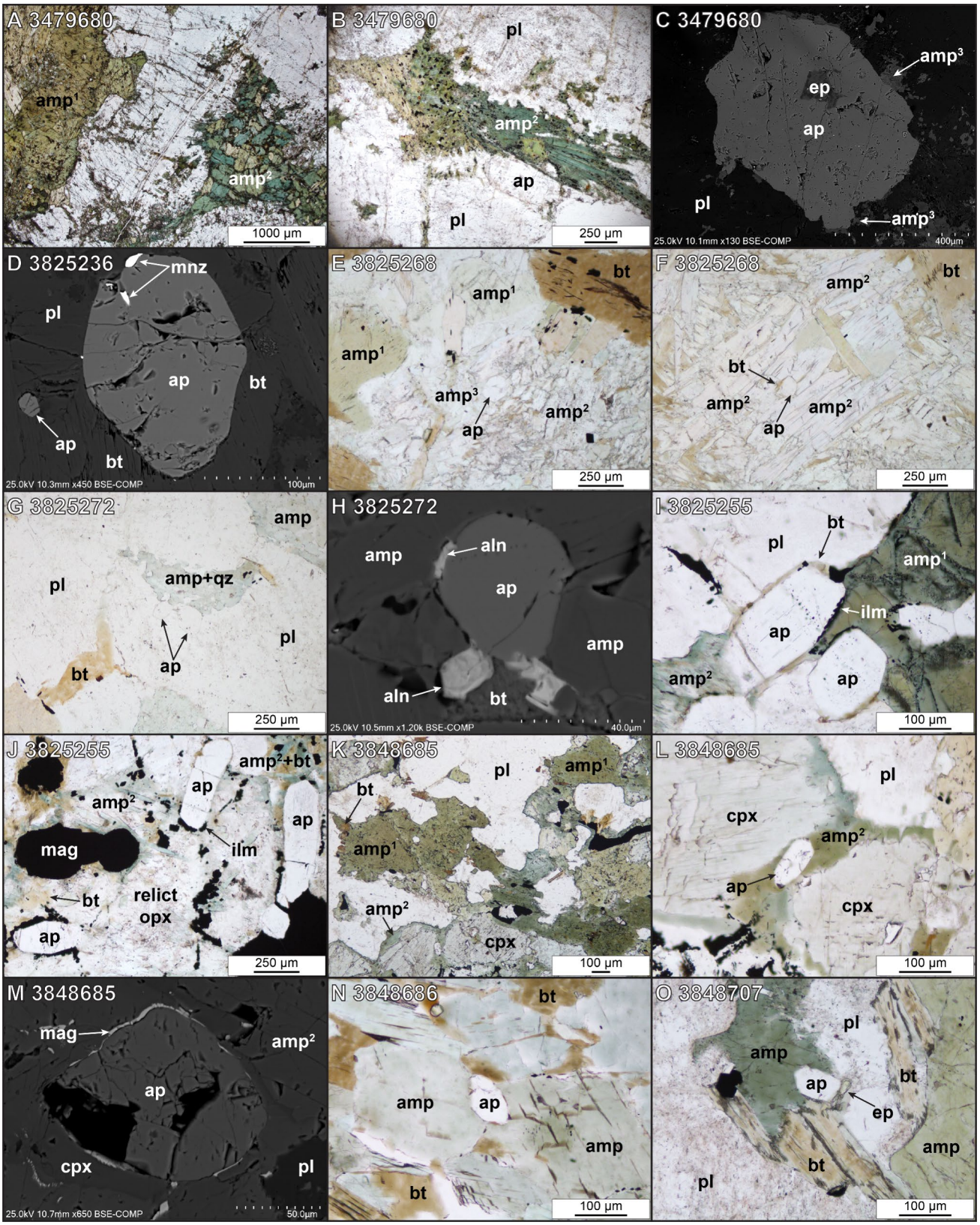
A 3479680
amp1
amp2
1000 µm
B 3479680
pl
amp2
ap
pl
250 µm
C 3479680
amp3
ep
ap
pl
amp3
25.0kV 10.1mm x130 BSE-COMP
400µm
D 3825236
mnz
pl
ap
bt
ap
bt
25.0kV 10.3mm x450 BSE-COMP
100µm
E 3825268
bt
amp1
amp1
amp3
ap
amp2
250 µm
F 3825268
amp2
bt
bt
amp2
ap
amp2
250 µm
G 3825272
amp
pl
amp+qz
pl
bt
ap
250 µm
H 3825272
amp
aln
ap
amp
aln
bt
25.0kV 10.5mm x1.20k BSE-COMP
40.0µm
I 3825255
bt
pl
amp1
ilm
ap
amp2
ap
100 µm
J 3825255
amp2+bt
ap
amp2
ap
mag
ilm
bt
relict
opx
ap
250 µm
K 3848685
pl
amp1
bt
amp1
amp2
cpx
100 µm
L 3848685
pl
cpx
amp2
ap
cpx
100 µm
M 3848685
mag
amp2
ap
cpx
pl
25.0kV 10.7mm x650 BSE-COMP
50.0µm
N 3848686
bt
amp
ap
amp
bt
100 µm
O 3848707
pl
amp
ap
bt
ep
amp
bt
pl
100 µm

◂**Fig. 3** Photomicrographs and back-scattered electron (BSE) imagery of in-situ apatite and associated minerals, highlighting the textural relationships between apatite and amphibole. **A** Muckanippie, 3479680: green–brown amphibole (amp^1), blue-green amphibole (amp^2), and plagioclase. Blue-green amphibole overprints brown-green amphibole at the margin. **B** Muckanippie, 3479680: apatite associated with blue-green amphibole (amp^2). **C** Muckanippie, 3479680: apatite associated with plagioclase and overprinted at the margin by fine-grained amphibole (amp^3), with epidote occurring at the apatite margin and infilling fractures. **D** Skuse Hill, 3825236: apatite associated with biotite and overprinted by monazite shows micro-voids. **E**, **F** Skuse Hill, 3825268: apatite associated with the colourless amphiboles (amp^2, amp^3). **G** Skuse Hill, 3825272: apatite in direct contact and associated with the pale green amphibole which contains fine-grained quartz. **H** Skuse Hill, 3825272: apatite overprinted by fine-grained allanite, with fine-grained biotite occurring at the apatite margin. **I**, **J** North-west Christie, 3825255: apatite associated with comparatively coarse-grained green amphibole (amp^1) and fine-grained amphibole (amp^2). Ilmenite is concentrated at the apatite grain boundaries and very fine-grained biotite overprints apatite. **K** Aristarchus, 3848685: comparatively coarse-grained green amphibole (amp^1) in contact with relict clinopyroxene, which is overprinted by fine-grained amphibole (amp^2). **L** Aristarchus, 3848685: apatite associated with fine-grained amphibole ($amp.^2$) which overprints relict clinopyroxene. **M** Aristarchus, 3848685: fractured apatite with micro-voids rimmed by fine-grained magnetite. **N** Aristarchus, 3848686: apatite associated with pale green amphibole and fine-grained biotite. **O** South-west Tarcoola, 3848707: apatite associated with amphibole and biotite. Epidote sits at the margin of apatite. Mineral abbreviations after Whitney and Evans (2010)

amphibole (amp^2; Fig. 3A, B). A third textural generation of extremely fine-grained amphibole (amp^3) is intergrown with very fine-grained epidote. Apatite occurs in direct contact with plagioclase and blue-green amphibole (amp^2), with sharp boundaries between the phases. Apatite is also partially overprinted at the rim by an association of fine-grained amphibole (amp^3) and epidote, with epidote infilling fractures in the apatite (Fig. 3B, C). Apatite interiors commonly preserve micro-voids which likely reflect partial dissolution of the grains (Fig. 3C).

Skuse Hill region

Drill core samples 3825236 (SKUSE HILL 2, 70.39–71.54 m), 3825268 (BLACKFELLOW HILL 1, 90.19–91.83 m), and 3825272 (BLACKFELLOW HILL 1, 143.07–143.80 m) are from the Skuse Hill Region in the Christie Domain (Fig. 2; Table 1). Sample 3825236 is a medium- to coarse-grained two-pyroxene metapyroxenite with a moderate solid-state foliation and interstitial biotite and plagioclase (Figs. S1–S4). Apatite is in association with biotite and plagioclase, with very fine-grained amphibole and monazite occurring at the apatite grain margins (Fig. 3D). Some grains preserve internal micro-voids reflecting partial dissolution (Fig. 3D). In rare cases, apatite occurs within the pyroxenes along fine fractures. Samples 3825268 and 3825272 are weakly to moderately foliated biotite-bearing amphibolites which intrude garnet-biotite-feldspar-quartz migmatitic gneiss (Christie Gneiss) with relatively sharp contacts (Figs. S1–S4). Sample 3825268 contains three textural generations of amphibole, all of which are in association with fine- to medium-grained fibrous biotite. Fine- to medium-grained acicular to fibrous amphibole (amp^2) has polysynthetic twinning and replaces medium-grained subhedral to anhedral amphibole (amp^1), which is moderate to dark green in colour (Fig. 3E). Apatite showing micro-voids is overprinted at the margins by very fine-grained biotite and associated with fine-grained colourless amphibole (amp^3; Fig. 3F). In sample 3825272, medium-grained pale green amphibole has poorly developed grain boundaries and forms interconnected networks, with the poikiloblastic interiors intergrown with fine-grained quartz (Fig. 3G). Biotite generally occurs at the amphibole margins, forming subhedral to anhedral fine- to medium-grained aggregates. Rounded to ellipsoidal apatite which forms poor grain shapes due to partial replacement by very fine-grained biotite or amphibole is associated with amphibole (Fig. 3G) or occurs along fractures between plagioclase grains. Fine-grained allanite associated with fine-grained biotite overprints apatite at the rims (Fig. 3H).

Far north-west Christie Domain

Drill core sample 3825255 (NNL IL2 DDH 1, 114.30–115.38 m) is from the far north-west Christie Domain in the western Gawler Craton, proximal to the Karari Shear Zone (Fig. 2; Table 1). The sample is interpreted to be co-magmatic with c. 2490 Ma tonalite (i.e., Mobella Tonalite), which occurs in a nearby drillhole (NNL IL1 DDH 2; Reid et al. 2014). The sample is an unfoliated medium-grained amphibole-plagioclase-biotite-orthopyroxene-bearing metanorite. Pockets of K-feldspar-quartz granite are entrained in the metanorite at the margins (Figs. S1–S4). Amphibole is the primary mineral in the sample, preserved as both euhedral to subhedral medium-grained porphyroblasts (amp^1) and anhedral grains, which are comparatively fine-grained and texturally late (amp^2; Fig. 3I). Medium- to coarse-grained orthopyroxene is partially replaced by fine-grained amphibole (amp^2) and fine-grained biotite, while medium-grained biotite porphyroblasts appear in textural equilibrium with amphibole (amp^1). Rounded and equant to elongate apatite grains are armoured within amphibole (amp^1), and occur along fracture planes in plagioclase, orthopyroxene, and magnetite. It is common for apatite to occur in association with fine-grained biotite, amphibole (amp^2), and fine-grained ilmenite, with ilmenite occurring along fractures at the margins of apatite (Fig. 3I, J). Apatite also occurs at the rims of magnetite and very fine-grained biotite overprints apatite.

Table 2 Summary of zircon U–Pb and apatite U–Pb and Lu–Hf ages

Sample	Drillhole	Zircon U–Pb (Ma)	Age type	Apatite U–Pb (Ma) Apatite Lu–Hf (Ma)	Age type
3479680	–	–	–	1621 ± 8	Thermal resetting (A)
				1732 ± 42**	Primary or recrystallisation
3825236	SKUSE HILL 2	2462 ± 2*	Metamorphic	1689 ± 20	Recrystallisation
		2430 ± 2*	Metamorphic	1735 ± 56	Recrystallisation
		2408 ± 3*	Metamorphic	–	–
3825255	NNL IL2 DDH 1	–	–	1713 ± 17	Thermal resetting
				2158 ± 119	Thermal resetting (A)
3825268	BLACKFELLOW HILL 1	2453 ± 3*	Metamorphic	1636 ± 10	Thermal resetting (A)
		2426 ± 2*	Metamorphic	1711 ± 39	Recrystallisation
3825272	BLACKFELLOW HILL 1	2469 ± 3	Magmatic	1637 ± 13	Thermal resetting (A)
		2438 ± 6	Metamorphic	1857 ± 82	Recrystallisation (A)
3848685	DMDD-001	2479 ± 12	Magmatic	1595 ± 16	Thermal resetting
		2430 ± 7	Metamorphic	1666 ± 50	Recrystallisation
3848686	DMDD-001	2467 ± 8	Magmatic	1590 ± 25	Thermal resetting
		2424 ± 10	Metamorphic	1632 ± 47	Recrystallisation
3848707	BGDDH 4	2471 ± 4*	Magmatic	1667 ± 9	Thermal resetting or recrystallisation
		2443 ± 11*	Metamorphic	1748 ± 59	Thermal resetting or recrystallisation

See discussion section for interpretation of age type. (A) indicates the apatite age is apparent. (*) Zircon U–Pb ages calculated using the Isoplot generated mixture modelling algorithm of Sambridge and Compston (1994), whereas others are $^{207}Pb/^{206}Pb$ weighted mean ages. (**) Lu–Hf isochron ages, whereas others are common Hf corrected $^{176}Hf/^{176}Lu$ weighted mean ages

Aristarchus prospect

Drill core samples 3848685 (DMDD-001, 193.00–194.43 m) and 3848686 (DMDD-001, 214.43–216.08 m) are from the Aristarchus prospect in the Christie Domain of the central Gawler Craton (Fig. 2; Table 1). Sample 3848685 is a weakly to moderately foliated fine- to medium-grained metagabbro comprising plagioclase, clinopyroxene, and amphibole, with the sample interlayered with foliated pale-white felsic material (Figs. S1, S2). Sample 3848686 is a weakly foliated biotite-bearing amphibolite which intrudes foliated felsic material with sharp contacts (Figs. S1–S4). In sample 3848685, clinopyroxene appears augitic and exhibits pervasive replacement textures to fine-grained pale green-tan amphibole (amp^2) and lesser chlorite. A possible earlier textural generation of fine- to medium-grained amphibole is also present in the sample and is overprinted at the margin by fine-grained biotite (amp^1; Fig. 3K). Fine-grained texturally late amphibole (amp^2) forms pseudomorphs after augite and corona textures around ilmenite, and is partially replaced by fine-grained biotite. Sub-rounded and equant to elongate apatite is most commonly associated with fine-grained amphibole (amp^2) at the margins of relict clinopyroxene and ilmenite, with grains rimmed by very fine-grained biotite and magnetite (Fig. 3L). Some apatite grains show pervasive fracturing and micro-voids which are likely indicative of partial dissolution (Fig. 3M). In sample 3848686, fine- to medium-grained pale green amphibole with poor grain shapes pseudomorphs clinopyroxene, although relict clinopyroxene grain shapes and cleavage planes are present. Sub-rounded and near-equant to ellipsoidal fine-grained apatite is typically preserved in association with amphibole and biotite, with grains overprinted at the rims by fine-grained fibrous biotite (Fig. 3N).

South-west of Tarcoola goldfield

Drill core sample 3848707 (BGDDH 4, 109.92–110.70 m) is located to the south-west of the Tarcoola Goldfield near the border of the Wilgena and Harris Greenstone domains in the central Gawler Craton (Fig. 2; Table 1). The sample is a weakly foliated medium- to coarse-grained amphibole-biotite diorite which is sharply cut by 1–15 cm wide granitic veins (Figs. S1–S4). Dark green to tan-brown amphibole is associated with fine- to medium-grained fibrous biotite, with grains commonly interconnected, forming agglomerates separated by medium-grained plagioclase. Amphibole is overprinted by another textural generation of biotite and can be associated with fine-grained euhedral monazite. Fine-grained ellipsoidal apatite occurs at the margins of, and along fractures within amphibole (Fig. 3O). It is common for apatite to form part of an association of fine-grained biotite, epidote, and chalcopyrite.

Analytical methods

Electron Probe Microanalysis (EPMA)

Major element oxide compositions of amphibole in seven of eight samples were measured using a CAMECA SXFive electron microprobe at Adelaide Microscopy, the University of Adelaide for the purpose of Ti-in-amphibole thermometry. Sample 3825236 does not contain amphibole. A beam current of 20 nA, a beam diameter of 2 µm, and an accelerating voltage of 15 kV were the operating conditions. Calibration procedures were undertaken on Astimex Pty Ltd synthetic and natural standards. Data reduction was performed in the Probe for EPMA software package by Probe Software Inc. Amphibole compositions and Ti-in-amphibole calculated temperatures are given in supplementary material 2. Temperatures were calculated following the method of Liao et al. (2021) for calcium amphibole. Amphibole end-member classification follows the scheme of Hawthorne et al. (2012).

Zircon SHRIMP U–Pb geochronology

Extended zircon SHRIMP data acquisition methods, including acquired ages for OGC1 and isotopic data for both OGC1 and 91500, are provided in supplementary material 3. Zircon was recovered from six of eight samples. Sample 3479680 from the Muckanippie region and sample 3825255 from the far north-west Christie Domain did not yield zircon.

Isotopic analyses were undertaken using a sensitive high resolution ion microprobe (SHRIMP II B) at the John de Laeter Centre, Curtin University, Perth. Differential fractionation between U and Pb was corrected by reference to a $^{206}Pb/^{238}U$ ratio of 0.1792 for interspersed analyses of the 91500 zircon standard (1062.4 ± 0.4 Ma; Wiedenbeck et al. 1995). Additionally, 91500 zircon was used for the calibration of elemental U concentrations (81.2 ppm U). The OGC1 zircon standard ($^{207}Pb/^{206}Pb = 0.29907 \pm 0.00011$, 3465.4 ± 0.6 Ma) was used to monitor $^{207}Pb/^{206}Pb$ reproducibility and accuracy (Stern et al. 2009). Samples were dated over three analytical sessions. Data were processed using the SQUID 2.5 software of Ludwig (2009). All data from individual analyses are tabulated with 1σ uncertainty. Data are plotted using IsoplotR (Vermeesch 2018) and displayed with 2σ uncertainties. Individual analyses omitted based on extensive common Pb typically had common ^{206}Pb concentrations greater than ~ 0.5%. A discordance filter of 5% was applied to the data.

Apatite multi-method isotopic analysis

Apatite U–Pb isotopes and both trace and rare earth element (REE) compositions, were acquired using laser-ablation inductively-coupled-plasma mass spectrometry (LA–ICP–MS) at Adelaide Microscopy. Lu–Hf isotopic compositions were measured using laser-ablation tandem inductively-coupled-plasma mass spectrometry (LA–ICP–MS/MS). Both methods utilised a RESOlution 193 nm Excimer laser-ablation system coupled to Agilent 8900 ICP–MS/MS. For U–Pb analysis, apatite grains were ablated using a spot size of 30 µm. For Lu–Hf analysis, grains were ablated using spot sizes of 67 µm and 120 µm. Extended analytical procedures, including operational parameters and details of calibration calculations, are provided in supplementary material 4. A summary of the apatite reference material ages and isotopic ratios for the U–Pb and Lu–Hf systems, including a comparison with published ages and ratios, is provided in supplementary material 5.

Apatite U–Pb isotopes and REE compositions were measured following the method described in Glorie et al. (2019). U–Pb data were corrected for mass bias, elemental fractionation, and instrument drift using primary reference material Madagascar apatite (Thomson et al. 2012). 401 apatite (Thompson et al. 2016) and Mt McClure apatite (Schoene and Bowring 2006) were used as secondary reference materials to test the accuracy of the method. The secondary reference materials yield ages consistent with published ages (supplementary material 5). Apatite $^{207}Pb/^{206}Pb$ ratios and both trace and REE concentrations were calibrated to synthetic glass standard NIST-610 (Jochum et al. 2011). REE data was used to construct chondrite-normalised REE plots. Data reduction was undertaken using LADR software (Norris and Danyushevsky 2018). In six of eight samples, apatite U–Pb lower-intercept linear regression ages were constrained by initial common Pb ($^{207}Pb/^{206}Pb_o$) compositions determined from plagioclase.

Lu–Hf isotopic compositions were measured following the method of Simpson et al. (2021). Lu–Hf ratios were calculated using a two-stage normalisation procedure. First, the ratios were normalised to synthetic glass standard NIST-610 using LADR (Nebel et al. 2009; Norris and Danyushevsky 2018). Lu–Hf ratios were then normalised so that the 'pseudo-primary' reference material OD306 (Thompson et al. 2016) yielded the correct age to account for laser induced elemental fractionation (e.g., Simpson et al. 2021). A session-dependent correction factor of ~ 3.60% was applied to the $^{176}Lu/^{177}Hf$ ratios of all unknowns and is based on the difference between (1) the calculated lower-intercept age of an inverse regression through the OD306 analyses (1656.3 ± 11.5 Ma) and (2) the expected lower-intercept age based on the published age (1596.7 ± 7.1 Ma;

Thompson et al. 2016). In-house reference apatite Bamble was also monitored as a secondary standard for accuracy checks (Simpson et al. 2021) and yielded a Lu–Hf age of 1101.8 ± 7.3 Ma. A small selection of trace and rare earth elements were measured concurrently with Lu–Hf isotopes (supplementary material 4, 8).

In order to produce $^{176}Hf/^{176}Lu$ single spot ages, common Hf corrections were applied to the apatite unknowns following Simpson et al. (2021). The correction uses the ^{178}Hf measured in a given sweep cycle to estimate the contribution of non-radiogenic (common) ^{176}Hf to the measured ^{176}Hf signal (e.g., Simpson et al. 2021). The correction was applied to the unknowns following background corrections, but prior to normalisation to the calibration standard (OD306). An initial $^{176}Hf/^{178}Hf$ ratio of 0.192 ± 0.004 was used for the correction, which is determined from the $^{176}Hf/^{177}Hf$ signature of typical crustal rocks (0.282 ± 0.004; Fisher and Vervoort 2018) and the fixed $^{177}Hf/^{178}Hf$ ratio of 0.682 (De Bievre and Taylor 1993). To avoid overcorrections in cases where initial Hf proportions in apatite are high, common Hf corrections were not applied to $^{177}Hf/^{176}Hf$ ratios exceeding 1 (e.g., Glorie et al. 2022). The difference between uncorrected and common Hf corrected single spot ages (% cHf corrected) is given in supplementary material 8. Inverse isochrons were used for the presentation of Lu–Hf data because conventional ratios have large and correlated uncertainties due to the low abundance of ^{177}Hf in apatite. Instead, inverse isochrons require ^{177}Hf as the numerator, using the ratios $^{177}Hf/^{176}Hf$ and $^{176}Lu/^{176}Hf$, resulting in data that is more easily interpreted (Li and Vermeesch 2021). The isochron regressions were anchored to an initial $^{177}Hf/^{176}Hf$ ratio of 3.55 ± 0.07 which encompasses the full range of variation in the lithospheric reservoir (e.g., Simpson et al. 2022; Glorie et al. 2023).

Results

Ti-in-amphibole thermometry

Figure. 4 shows the end-member classification for each textural generation of amphibole described in the petrography section (Fig. 3; supplementary material 1). Minimum, maximum, and average temperatures calculated using the titanium concentrations in calcium amphibole (Liao et al. 2021) are provided for each textural generation (Fig. 4; supplementary material 2). Each textural generation of amphibole, with the exception of cummingtonite in sample

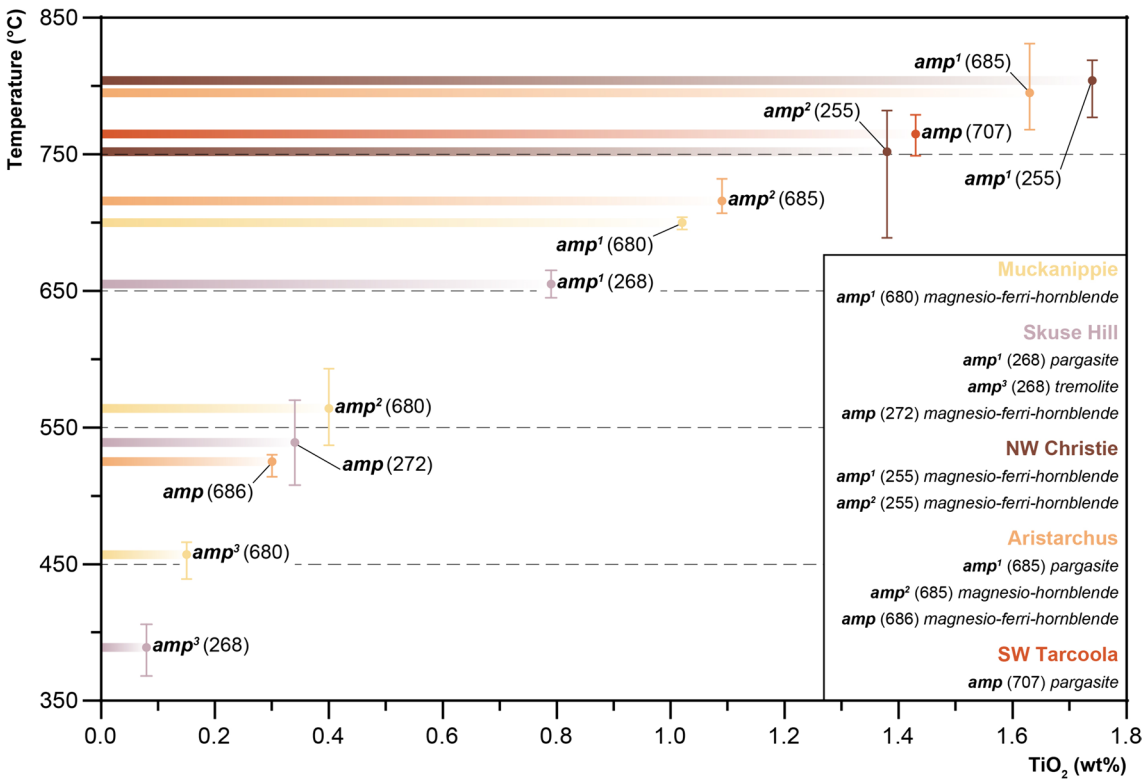

Fig. 4 Ti-in-amphibole thermometry: plot of Temperature (°C) against TiO_2 (wt%) for the different textural generations of amphibole. TiO_2 concentrations are mean values, with vertical bars indicating the minimum and maximum temperatures for each amphibole. TiO_2 concentrations and temperatures for all analyses are provided in supplementary material 2

3825268, has sufficient calcium according to the definition of calcium amphibole given by Liao et al. (2021), which is simplified from that of Hawthorne et al. (2012). Furthermore, ilmenite is present in each amphibole-bearing sample (Fig. 3; Table 1; supplementary material 1), and so use of the Ti-in-amphibole thermometer is deemed appropriate. Recorded amphibole temperatures are 695–704 °C (amp^1), 537–593 °C (amp^2), and 439–466 °C (amp^3) for sample 3479680, 645–665 °C (amp^1) and 368–406 °C (amp^3) for sample 3825268, 508–570 °C for sample 3825272, 777–819 °C (amp^1) and 689–782 °C (amp^2) for sample 3825255, 768–831 °C (amp^1) and 707–732 °C (amp^2) for sample 3848685, 514–530 °C for sample 3848686, and 749–779 °C for sample 3848707.

Zircon U–Pb isotopic data

Zircon U–Pb Tera–Wasserburg concordia plots, probability density distribution plots, and representative CL images are shown in Fig. 5. Supplementary material 6 contains the complete set of CL images and spot locations (Figs. S5–S10), and detailed descriptions of the morphological and internal characteristics of the zircons. An extended SHRIMP U–Pb results section is also included in supplementary material 6, which details the rationale for the age calculations and the treatment of outliers, and interpretations of inheritance and Pb loss. Data tables for the unknowns are provided in supplementary material 7.

Zircons in all six analysed samples record early Palaeoproterozoic ages (Fig. 5; supplementary material 6, 7). Samples 3825236 and 3825268 from the Skuse Hill region primarily contain interpreted metamorphic zircons, with near-equant to ellipsoidal grains with rounded terminations showing dark-CL homogenous cores or bright- to intermediate-CL cores with patchy zonation (Figs. 5A, B, S5, 6). Excluding analyses influenced by Pb loss or from inherited grains (supplementary material 6), the analyses from metamorphic zircons return ages between c. 2470–2405 Ma (Fig. 5A–D). A probability density distribution of the metamorphic analyses in sample 3825236 shows two primary peaks and two subordinate peaks (Fig. 5C), with the Isoplot generated mixture modelling algorithm of Sambridge and Compston (1994) calculating ages of 2408 ± 3 Ma (14% of analyses), 2430 ± 2 Ma (31% of analyses), 2444 ± 2 Ma (22% of analyses), and 2462 ± 2 Ma (33% of analyses) for the four peaks. It is possible all four ages reflect discrete metamorphic events. Another possibility is that the two primary peaks correspond to metamorphic episodes at c. 2462 Ma and c. 2430 Ma and the intermediate peak at c. 2444 Ma is an apparent peak produced by overlap of the main peaks. The metamorphic population in sample 3825268 is assumed to be bimodal, with the mixture modelling algorithm producing ages of 2426 ± 2 Ma (71% of analyses) and 2453 ± 3 Ma (29% of analyses; Fig. 5D).

Sample 3825272 from the Skuse Hill region, samples 3848685 and 3848686 from the Aristarchus prospect, and sample 3848707 from south-west of Tarcoola contain zircons interpreted to be both magmatic and metamorphic based on morphologies and zoning patterns (Figs. 5E, F, I, J; S7–S10). In sample 3825272, the analyses defining the primary peak (Fig. 5G) correspond with dark-CL cores recording comparatively high $^{232}Th/^{238}U$ ratios exceeding 1. In contrast, the analyses defining the broad peak represent bright-CL rims and grains with low $^{232}Th/^{238}U$ ratios of 0.17–0.36 (Fig. 6A). The analyses from interpreted magmatic dark-CL cores return a $^{207}Pb/^{206}Pb$ weighted mean age of 2469 ± 3 Ma (MSWD = 0.87; POF = 0.60; n = 17; Figs. 5G, 6A). The analyses from bright-CL rims and grains return a $^{207}Pb/^{206}Pb$ weighted mean age of 2438 ± 6 Ma (MSWD = 1.30; POF = 0.20; n = 16; Figs. 5G, 6A). Similarly, analyses from sample 3848686 show a coupling between age and Th/U composition, with analyses corresponding with interpreted magmatic dark- to intermediate-CL homogenous or patchy zoned cores recording high $^{232}Th/^{238}U$ ratios (0.80–1.22) and returning a $^{207}Pb/^{206}Pb$ weighted mean age of 2467 ± 8 Ma (MSWD = 1.60; POF = 0.07; n = 17; Figs. 5K, 6B). In contrast, analyses from interpreted metamorphic bright- to intermediate-CL rims and grains showing sector and patchy zoning have $^{232}Th/^{238}U$ ratios of 0.57–0.89 and yield a $^{207}Pb/^{206}Pb$ weighted mean age of 2424 ± 10 Ma (MSWD = 1.16; POF = 0.31; n = 12; Figs. 5K, 6B). Zircons from sample 3848685 have similar morphological and internal features to those in sample 3848686 (Figs. 5F, I; S8, 9). The oldest analyses correspond with bright- to intermediate-CL broadly zoned zircons, which are interpreted as magmatic cores. In contrast, the younger analyses forming the dominant peak typically correlate with dark- to intermediate-CL variably zoned metamorphic rims. The inferred magmatic population returns a $^{207}Pb/^{206}Pb$ weighted mean age of 2479 ± 12 Ma (MSWD = 0.72; POF = 0.61; n = 5; Fig. 5H). The inferred metamorphic population yields a $^{207}Pb/^{206}Pb$ weighted mean age of 2430 ± 7 Ma (MSWD = 1.50; POF = 0.10; n = 19; Fig. 5H). In sample 3848707, many zircons have visible internal core-rim structures, suggesting that the age distribution harbours two populations comprising (1) cores and grains interpreted to be magmatic and (2) rims and grains interpreted to be metamorphic in origin (Fig. 5J; S10). The mixture modelling algorithm produces ages of 2471 ± 4 Ma (79% of analyses) and 2443 ± 11 Ma (21% of analyses) for the cores and rims, respectively (Fig. 5J, L).

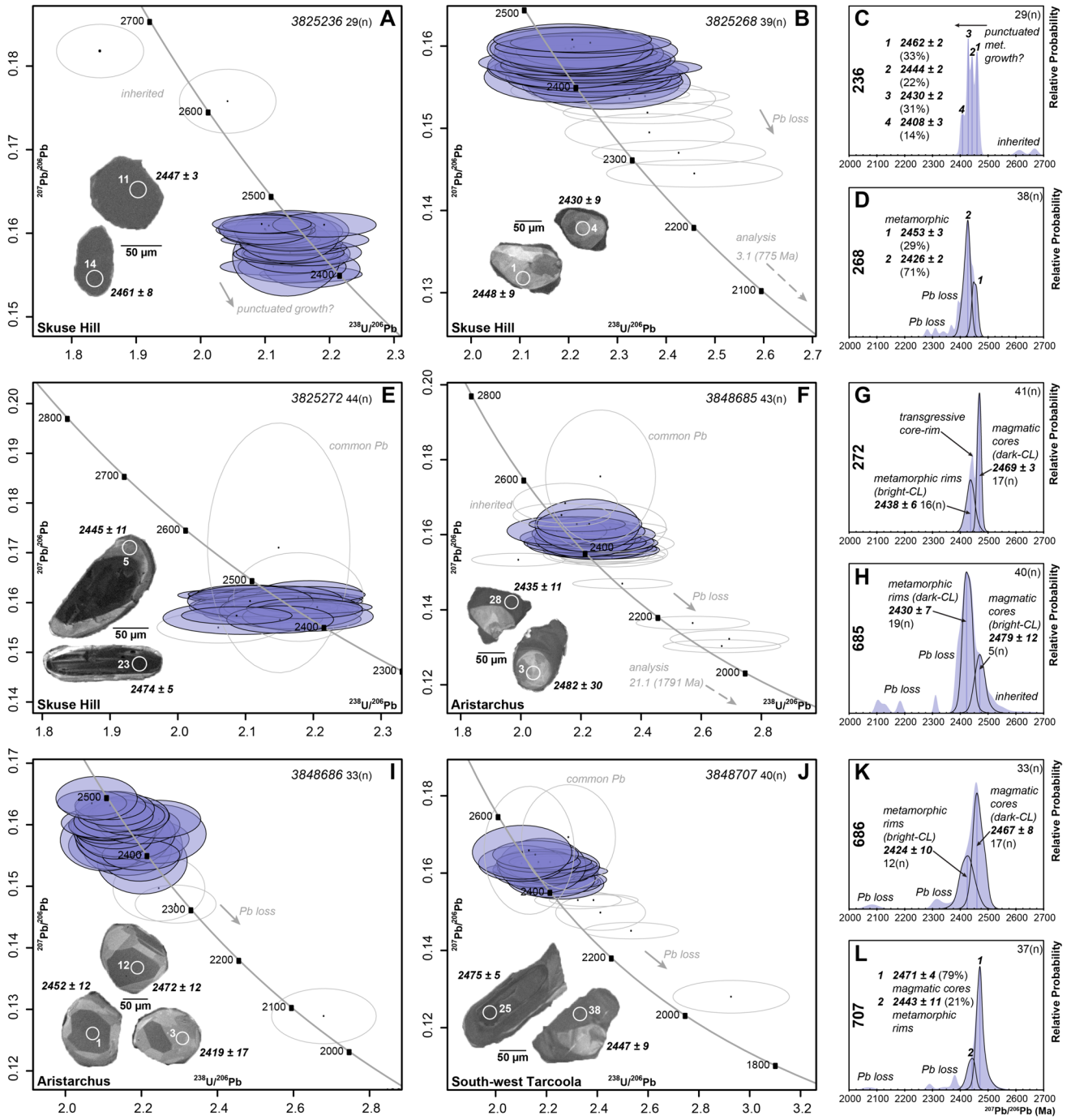

Fig. 5 Zircon SHRIMP U–Pb Tera–Wasserburg concordia plots and probability density distribution plots. Shown on each concordia plot are representative cathodoluminescence (CL) images for zircon, with spot locations annotated on the zircon grains. Quoted ages are $^{207}Pb/^{206}Pb$ (Ma). The complete set of CL images is provided in supplementary material 6. Annotated on the probability density distribution plots are either $^{207}Pb/^{206}Pb$ weighted mean ages or Isoplot generated mixture modelling ages (Sambridge and Compston 1994) for interpreted discrete populations

Apatite U–Pb isotopic data

The apatite U–Pb data are presented on Tera–Wasserburg concordia plots in Fig. 7. Unfilled ellipses have been omitted on the basis of inclusion-related contamination. U–Pb isotopic data and ages for the unknowns are given in supplementary material 8.

Ages quoted in black text are derived from linear regressions anchored to initial $^{207}Pb/^{206}Pb$ compositions determined from plagioclase. For comparison, ages quoted

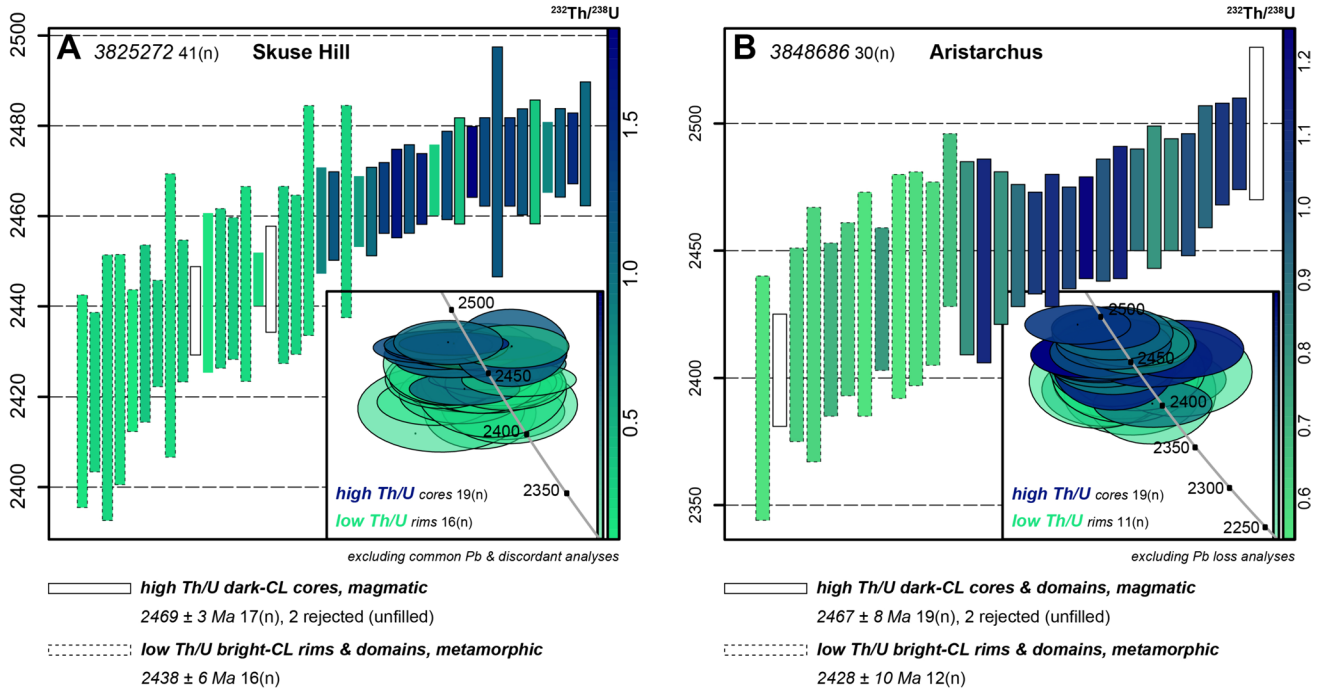

Fig. 6 $^{207}Pb/^{206}Pb$ ages for zircon in samples 3825272 (**A**) and 3848686 (**B**). The plots highlight the variation in $^{232}Th/^{238}U$ with age, with comparatively high $^{232}Th/^{238}U$ ratios typically corresponding with zircon cores

in green text are unanchored (Fig. 7). With the exception of sample 3479680, it is not clear whether apatite and plagioclase are in textural equilibrium (Fig. 3). However, anchored and unanchored linear regression ages are similar and within uncertainty in each sample (the maximum difference between these ages is 1.2%), which indicates the choice of initial Pb reservoir makes little difference to the calculated ages.

Apatite U–Pb lower-intercept linear regression ages are between c. 1710–1590 Ma for all samples (Fig. 7). Uncertainties on the final ages for all samples range from 0.5% to 1.2% (anchored regressions) and from 0.6% to 1.9% (unanchored regressions). $(^{207}Pb/^{206}Pb)_o$ compositions range from 0.892 to 1.036 for anchored regressions and 0.862 to 1.062 for unanchored regressions (Fig. 7). Apatite in sample 3825255 from the far north-west Christie Domain yields the oldest U–Pb age of 1713 ± 17 Ma (MSWD = 1.00; Fig. 7E). Apatite in samples 3848685 and 3848686 from the Aristarchus prospect return the youngest ages of 1595 ± 16 Ma (MSWD = 2.60; Fig. 7F) and 1590 ± 25 Ma (MSWD = 2.40; Fig. 7G), respectively. The remaining samples give apatite U–Pb ages of 1621 ± 8 Ma (sample 3479680, Muckanippie region; MSWD = 1.20; Fig. 7A), 1689 ± 20 Ma (sample 3825236, Skuse Hill; MSWD = 2.90; Fig. 7B), 1636 ± 10 Ma (sample 3,825,268, Skuse Hill; MSWD = 1.20; Fig. 7C), 1637 ± 13 Ma (sample 3,825,272, Skuse Hill; MSWD = 2.20; Fig. 7D), and 1667 ± 9 Ma (sample 3848707, south-west of Tarcoola; MSWD = 1.20; Fig. 7H).

Apatite Lu–Hf isotopic data

Inverse Lu–Hf isochrons for apatite in all samples are presented in Fig. 8. Analyses with ellipses in blue have $^{177}Hf/^{176}Hf$ ratios < 1, which have been used to calculate common Hf corrected $^{176}Hf/^{176}Lu$ single spot ages (analytical methods section). Unfilled ellipses have been omitted on the basis of contamination or $^{176}Hf/^{177}Hf$ values below detection. Common Hf corrected $^{176}Hf/^{176}Lu$ weighted mean ages are provided for each sample (Fig. 8). Lu–Hf isotopic data and ages for the unknowns are given in supplementary material 8.

Apatite from all samples contains highly radiogenic Lu–Hf ratios (Fig. 8) except for apatite in sample 3479680 from the Muckanippie region, which shows a comparatively large spread in $^{177}Hf/^{176}Hf$ ratios (Fig. 8A). Hence, with the exception of sample 3479680 which returns a Lu–Hf isochron age of 1732 ± 42 Ma (MSWD = 1.60), the common Hf corrected $^{176}Hf/^{176}Lu$ weighted mean ages are used in further discussion (Fig. 8B–H). Uncertainties on the final ages for all samples range from 2.3% to 5.5%, with an average of 3.4%. $^{176}Hf/^{176}Lu$ weighted mean ages for samples 3825236 and 3825268 from the Skuse Hill region, and sample 3848707 from south-west of Tarcoola,

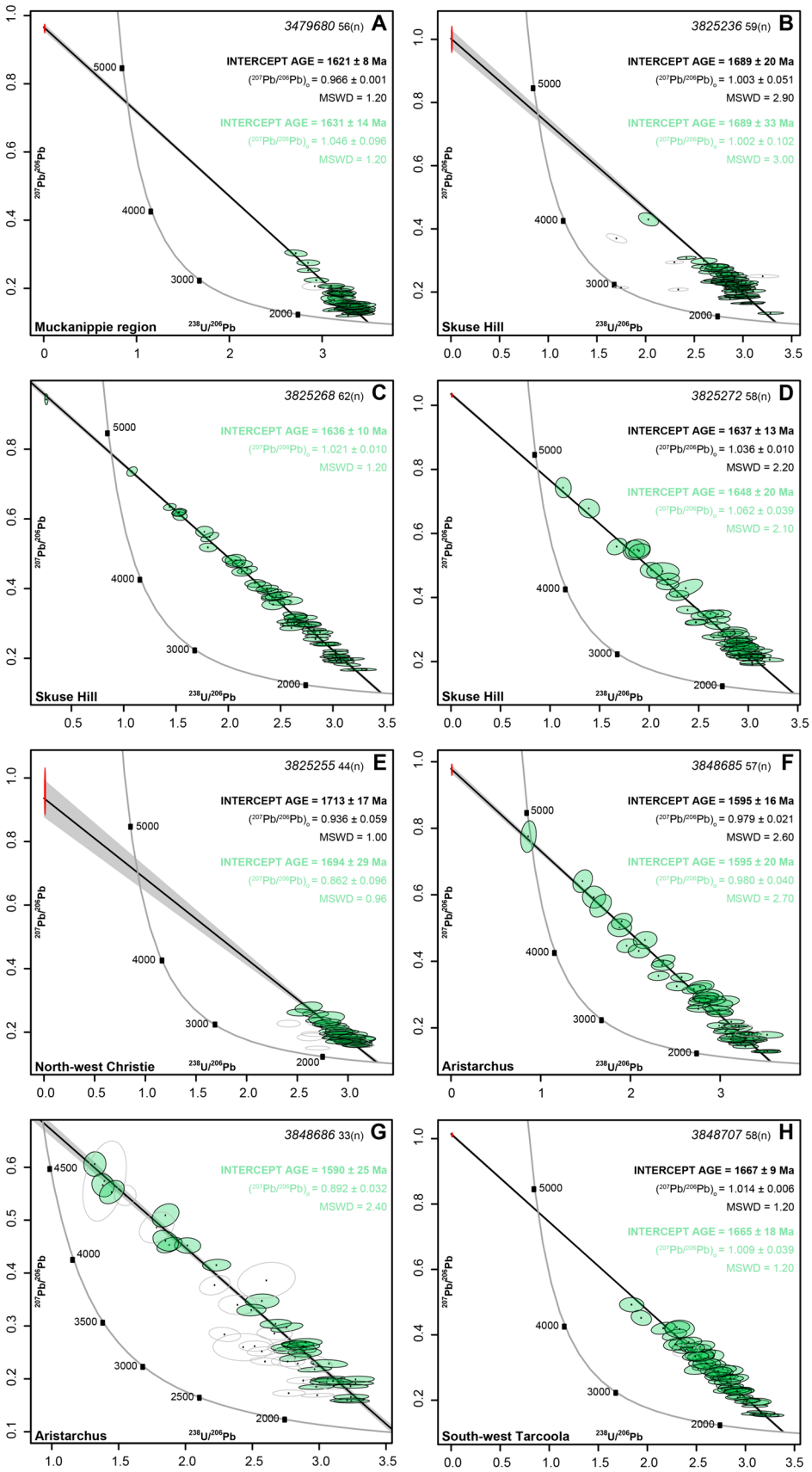

Fig. 7 Apatite LA–ICP–MS U–Pb Tera–Wasserburg concordia plots for each sample. The intercept ages quoted in black text are anchored to $^{207}Pb/.^{206}Pb$ compositions determined from plagioclase (red bars) whereas the ages given in green text are unanchored. Unfilled uncertainty ellipses (2σ) represent those excluded from the age calculations (see text)

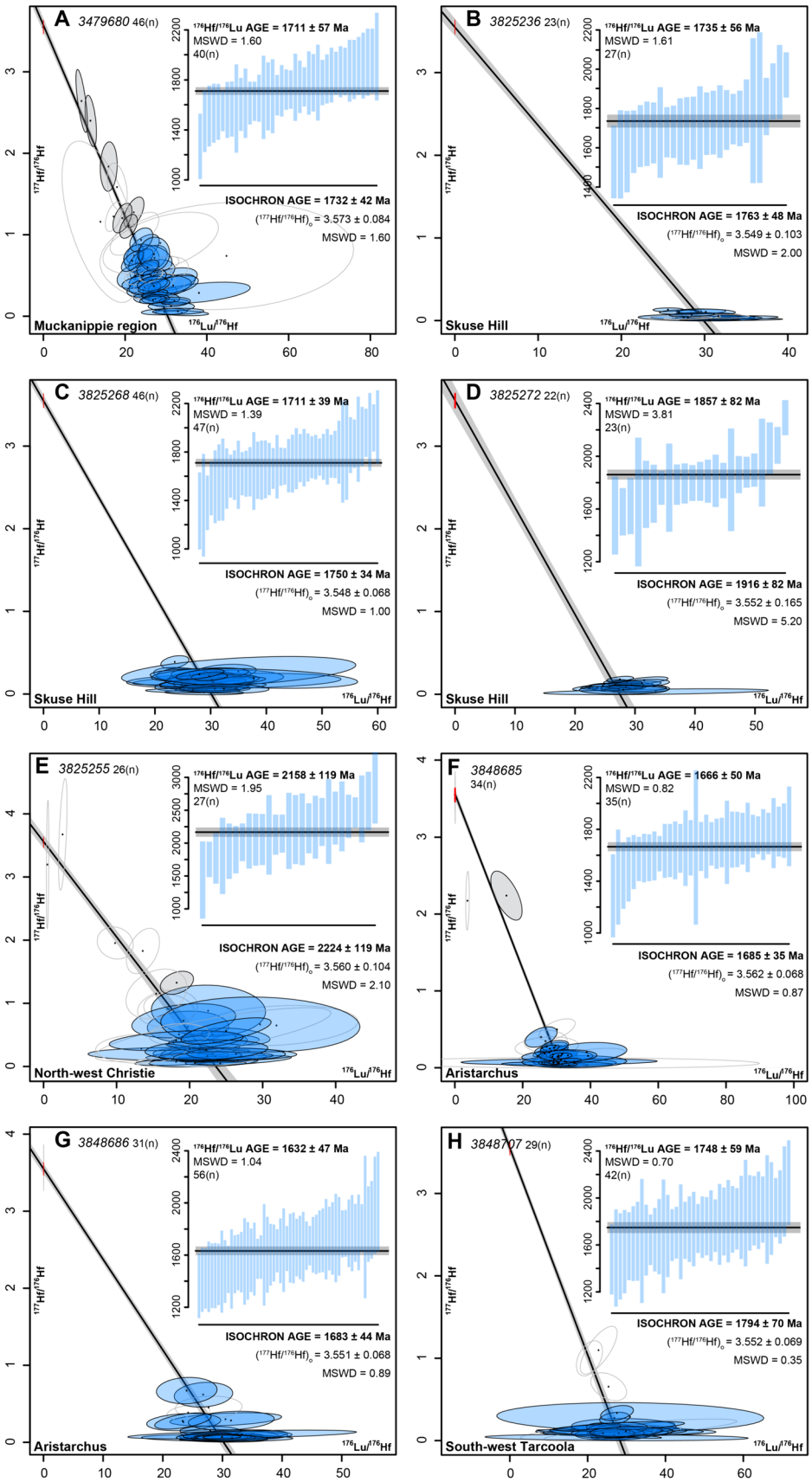

Fig. 8 Apatite LA–ICP–MS/MS Lu–Hf isochrons. The isochron regressions were anchored to an initial $^{177}Hf/^{176}Hf$ ratio of 3.55 ± 0.07 (red bars). For each isochron, the inset shows common Hf corrected $^{176}Hf/^{176}Lu$ single spot ages. Grey uncertainty ellipses are not included in the $^{176}Hf/.^{176}Lu$ weighted mean age calculations given a common Hf correction was not applied to these analyses. Unfilled uncertainty ellipses (2σ) represent those excluded from the age calculations (see text)

are between c. 1750–1710 Ma and agree within uncertainty (MSWD = 0.70–1.61; Fig. 8B, C, H). Sample 3825272 from the Skuse Hill region gives a slightly older $^{176}Hf/^{176}Lu$ weighted mean of 1857 ± 82 Ma with a corresponding high MSWD of 3.81, indicating the analyses have excess scatter beyond their analytical uncertainties, and therefore do not conform to a single population at the 95% confidence level (Fig. 8D). However, if the two oldest analyses are omitted from the calculation (based on the outlier rejection function in IsoplotR), a younger and more precise $^{176}Hf/^{176}Lu$ weighted mean age of 1806 ± 54 Ma (MSWD = 1.27) is produced, with its uncertainty overlapping with the ages from similar Skuse Hill samples 3825236 and 3825268. Therefore, the older date of 1857 ± 82 Ma (MSWD = 3.81) is conceivably an apparent date and not associated with a geological event. Apatite from sample 3825255 from the far north-west Christie Domain yields the oldest $^{176}Hf/^{176}Lu$ weighted mean of 2158 ± 119 Ma (MSWD = 1.95; Fig. 8E). With dispersion in the data and a reasonably high MSWD indicating the analyses have excess scatter beyond their analytical uncertainties, the date is interpreted as apparent and not geologically meaningful. Apatite from samples 3848685 and 3848686 from the Aristarchus prospect return the youngest $^{176}Hf/^{176}Lu$ weighted mean ages of 1666 ± 50 Ma (MSWD = 0.82) and 1632 ± 47 Ma (MSWD = 1.04), respectively (Fig. 8F, G).

Apatite rare earth element data

Apatite chondrite-normalised REE plots and Sr/Y versus ∑light-REE (LREE) discrimination plots (O'Sullivan et al. 2020) are presented in Fig. 9. REE data are provided in supplementary material 8.

Apatite in most samples have strong to weak negatively sloping mid- to heavy-REE trends, with trends in samples 3825268 (Skuse Hill region) and 3848685 (Aristarchus prospect) appearing near-flat (Fig. 9C, F). Apatite light- to mid-REE trends are near-flat in samples 3479680 (Muckanippie region) and 3825255 (far north-west Christie Domain; Fig. 9A, E), positively sloping in samples 3825236 (Skuse Hill region) and 3848707 (south-west of Tarcoola; Fig. 9B, H), and negatively sloping in sample 3825268 (Skuse Hill region; Fig. 9C). Considerable dispersion is apparent in the apatite light- to mid-REE data from Skuse Hill sample 3825272 and Aristarchus samples 3848685 and 3848686 (Fig. 9D, F, G). The most strongly negative Eu anomalies are apparent in apatite from Skuse Hill sample 3825236 (Fig. 9B).

Apatite analyses for most samples plot in the mafic field on a Sr/Y versus ∑LREE discrimination plot, with a proportion of analyses in samples 3825272, 3848685, 3848686, and 3848707 occurring in the low-grade metamorphic/metasomatic field (Fig. 9D, F–H). Apatite analyses in sample 3825268 plot in the ultramafic field on a Sr/Y versus ∑LREE discrimination plot (Fig. 9C).

Discussion

Early Palaeoproterozoic mafic magmatism

Zircon SHRIMP U–Pb geochronology reveals the samples in this study record early Palaeoproterozoic mafic magmatism. The zircon cores exhibit oscillatory zoning and return unimodal populations, supporting a magmatic origin. In addition, the mafic rocks intrude the metasedimentary Christie Gneiss and, at the Aristarchus prospect, are associated with the c. 2475–2470 Ma Aurora Tank Suite (which also intrudes the Christie Gneiss; Williams and Reid 2021).

The four magmatic ages recovered from Mulgathing Complex samples in both the Christie Domain (samples 3825272, 3848685, 3848686) and the Wilgena Domain (sample 3848707) range between c. 2479–2467 Ma, and agree within analytical uncertainty. For sample 3825255 without zircon geochronology, it is inferred that the crystallisation age is early Palaeoproterozoic based on the geochronological results from lithologically similar samples in this study and the observation that the mafic rock is in textural equilibrium with c. 2490 Ma tonalite (Mobella Tonalite; Reid et al. 2014). For Muckanippie Anorthosite outcrop sample 3479680 without zircon data, the intrusion age is uncertain given the absence of field relationships. However, as revealed by Total Magnetic Intensity (TMI) imagery (Fig. 2), outcropping Muckanippie Suite is associated with a circular body of low to moderate magnetic amplitude (Direen et al. 2005), suggesting it intrudes, and therefore post-dates, Mulgathing Complex basement. Furthermore, a maximum crystallisation age for the anorthosite has been constrained to 1871 ± 4 Ma, with the very small zircon yield attributed to possible inheritance (Jagodzinski et al. 2006).

The c. 2479–2467 Ma ages are equivalent to granitic rocks of the Aurora Tank Suite and are coincident with the peak temperature phase of the granulite-facies Sleafordian Orogeny in the central-northern Gawler Craton (Halpin and Reid 2016). Therefore, the results from this study indicate the Aurora Tank Suite is a bimodal syn-metamorphic suite and is not restricted to felsic magmatism as previously thought (Williams and Reid 2021). Furthermore, these results build on the already established framework of extensional tectonics, basin development, and punctuated bimodal magmatism in the central-northern Gawler Craton spanning c. 2558–2467 Ma (Swain et al. 2005; Reid et al. 2014; Halpin and Reid 2016).

The interpreted metamorphic ages spanning c. 2462–2408 Ma recorded by the Mulgathing Complex mafic intrusions are in agreement with the c. 2475–2410 Ma

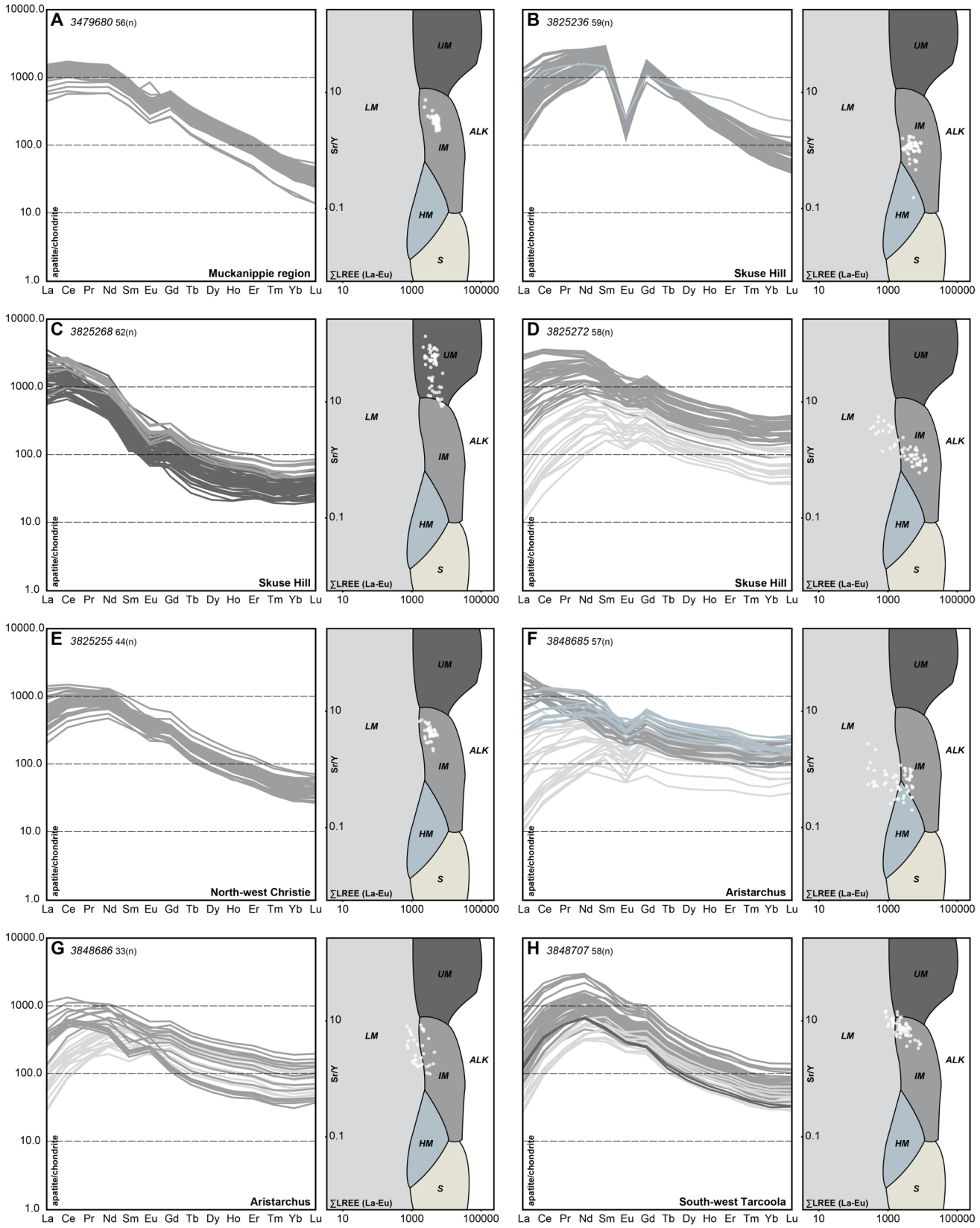

Fig. 9 Apatite chondrite-normalised REE plots and Sr/Y versus ∑LREE discrimination plots after O'Sullivan et al. (2020). Analyses are coloured according to their location on the Sr/Y versus ∑LREE discrimination plot. Normalisation values from Sun and McDonough (1989)

record of high thermal gradient metamorphism during the Sleafordian Orogeny in the central-western Gawler Craton (McFarlane 2006; Fanning et al. 2007; Jagodzinski et al. 2009; Reid et al. 2014; Halpin and Reid 2016; Jagodzinski and Reid 2017). A general pattern apparent in the zircon data from most samples is the small degree of interpreted Pb diffusion, which is possibly a result of later metamorphism and/or metasomatism associated with late Palaeo- to early Mesoproterozoic tectonism. The pervasive development of amphibole-dominant hydrous assemblages in most of the mafic intrusions (Figs. 3, S1−S4) has partially to completely erased the primary magmatic assemblages. This overprint is hypothesised to post-date the c. 2475–2410 Ma Sleafordian Orogeny. The apatite geochronology is a tool with which to test the hypothesis of a late Palaeoproterozoic hydrous overprint.

Apatite U–Pb and Lu–Hf decoupling

The apatite U–Pb and Lu–Hf systems largely record late Palaeoproterozoic ages which post-date the c. 2479–2467 Ma early Palaeoproterozoic emplacement ages recorded by the U–Pb system in zircon (Fig. 10). Additionally, apatite in each sample records U–Pb ages which are slightly younger than the ages produced by the Lu–Hf system (Fig. 10). For samples where the age of magmatic crystallisation is demonstrated as early Palaeoproterozoic (i.e., 3825236, 3825268, 3825272, 3825255, 3848685, 3848686, 3848707), these results suggest that apatite does not possess primary magmatic isotopic compositions and partial to complete open system behaviour of Pb and Hf (including dissolution-reprecipitation) occurred as a consequence of late Palaeoproterozoic tectonism.

In more detail, the apatite U–Pb ages are relatively variable, correlating with either the c. 1730–1690 Ma Kimban Orogeny (samples 3825236, 3825255, 3848707) or c. 1590–1575 Ma Hiltaba Suite magmatism (samples 3848685, 3848686), or falling between these two events (samples 3479680, 3825268, 3825272; Fig. 10). In contrast, the apatite Lu–Hf ages more exclusively correlate with the c. 1730–1690 Ma Kimban Orogeny and c. 1690–1670 Ma Tunkillia Suite (Fig. 10). The two samples from the Aristarchus prospect (3848685, 3848686) are the only samples in this study with U–Pb ages correlating directly

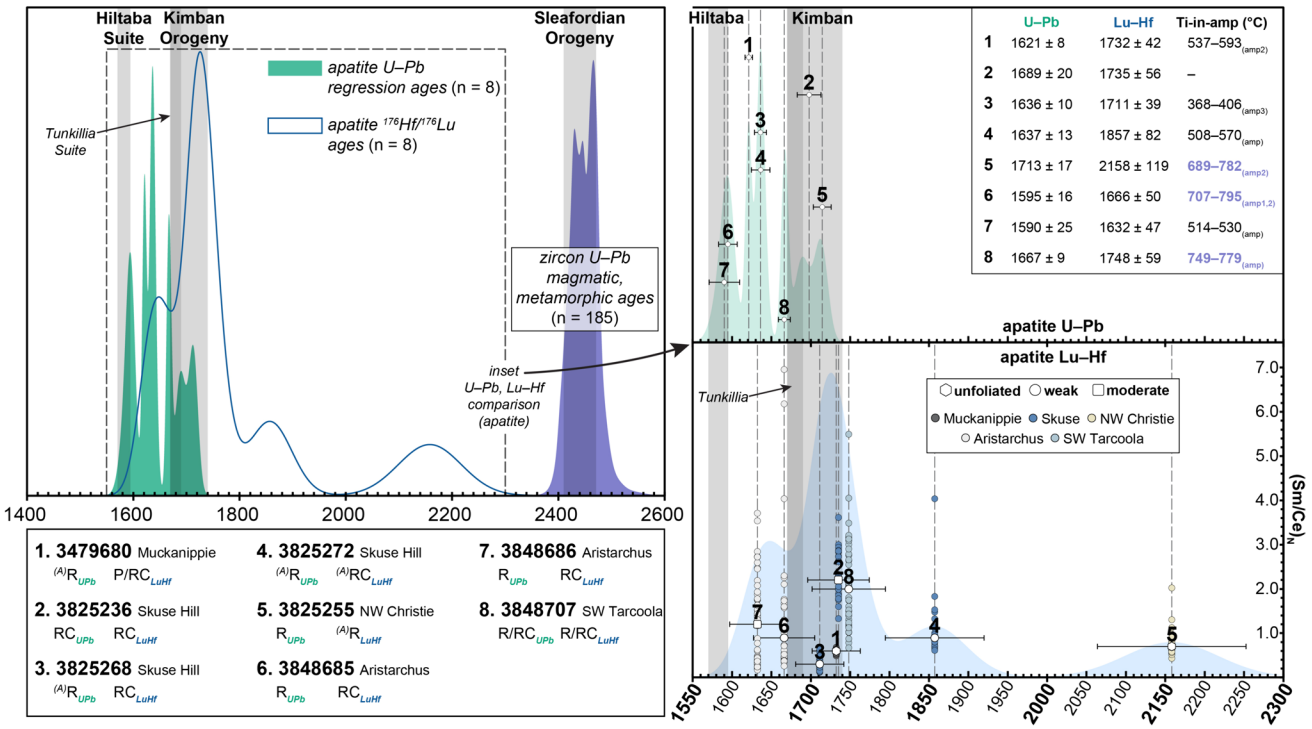

Fig. 10 Comparison of apatite U–Pb and Lu–Hf ages with zircon U–Pb ages in this study. The probability density distribution plots of the apatite data are derived from the U–Pb linear regression ages (green) and the $^{176}Hf/^{176}Lu$ weighted mean ages (blue), with the exception of sample 3479680 where the Lu–Hf isochron age was used. Uncertainties on all ages are 2σ. Quoted Ti-in-amphibole thermometry temperatures are from amphibole interpreted to be in textural equilibrium with apatite. Purple text indicates the amphibole generation may possibly be early Palaeoproterozoic (Sleafordian, refer to discussion). Chondrite-normalised Sm/Ce ratios are plotted against the apatite $^{176}Hf/^{176}Lu$ weighted mean ages as a proxy for light- to mid-REE patterns. Large symbols (white fill) represent median $(Sm/Ce)_N$ whereas coloured circles represent individual analyses. Sm and Ce concentrations (ppm) are from the Lu–Hf dataset. *P* primary age, *R* thermally re-equilibrated age, *RC* recrystallisation age. Superscript (A) indicates the age is apparent

with Hiltaba Suite magmatism, and they also record the youngest Lu–Hf ages of 1666 ± 50 Ma and 1632 ± 47 Ma, respectively (Fig. 10). While Hiltaba Suite granite is not documented in the immediate Aristarchus region, with the closest mapped pluton residing ~ 20 km to the south-west in the northern Fowler Domain (Fig. 1), these results provide evidence for otherwise undocumented c. 1590 Ma processes at the Aristarchus prospect. The Lu–Hf ages and uncertainties overlap with the range of ages for c. 1690–1670 Ma Tunkillia Suite magmatism suggesting probable correlation with this event, although because these ages are comparatively young (particularly the Lu–Hf age from sample 3848686), minor partial resetting due to Hiltaba-related processes cannot be ruled out. The two oldest apatite Lu–Hf ages of 2158 ± 119 Ma and 1857 ± 82 Ma recorded by samples 3825255 and 3825272 from the far north-west Christie Domain and Skuse Hill region, respectively, likely reflect partial resetting of the Lu–Hf system given the dispersion in the datasets and the relatively high MSWDs (Fig. 8D, E). Therefore, the ages are apparent ages and not geologically relevant.

Whereas the apatite U–Pb ages contemporaneous with late Palaeoproterozoic to early Mesoproterozoic (c. 1590–1575 Ma) tectonism probably reflect complete resetting, the intermediary ages are plausibly partially reset apparent ages. Solid-state diffusion promoted by c. 1590–1575 Ma Hiltaba-related thermal processes in the central Gawler region is the favoured mechanism for partial to complete Pb isotopic re-equilibration as it satisfies the observation of a post-Kimban unmodified Hf system in apatite, whereas the process of dissolution-reprecipitation presumably would have reset both Pb and Hf compositions. This interpretation is consistent with experimental data, with estimates for the Lu–Hf closure temperature in apatite between 660 and 730 °C (Cherniak 2000; Barfod et al. 2005; Chew and Spikings 2015; Glorie et al. 2023) and U–Pb closure temperature estimates between 375 and 550 °C (Schoene and Bowring 2007; Chew et al. 2011; Cochrane et al. 2014). Several other studies provide geochronological data that supports this relationship between the U–Pb and Lu–Hf systems (e.g., Barfod et al. 2005; Gillespie et al. 2022; Glorie et al. 2022, 2023; Kharkongor et al. 2023). These findings are also consistent with geochronological and experimental data that demonstrate a decoupling between the U–Pb and REE systems in apatite, with Pb diffusion persisting to lower temperatures than REE diffusion (Cherniak 2000; Kirkland et al. 2018; Odlum et al. 2022).

Apatite Lu–Hf re-equilibration: insights from petrological and compositional data

The apparent isotopic re-equilibration of the Lu–Hf system in apatite is either a consequence of Hf thermal volume diffusion or recrystallisation induced by metamorphism or metasomatism during the Kimban Orogeny. An interpretation of apatite recrystallisation facilitated by metamorphism relies on the premise that Kimban-aged retrogression of the c. 2479–2467 Ma mafic intrusive rocks was characterised by temperatures below 660–730 °C. If temperatures exceeded 660–730 °C, the Hf compositions in apatite may have been influenced by thermally activated volume diffusion (Barfod et al. 2005; Glorie et al. 2023). While temperature estimates for the Kimban Orogeny in the central Gawler Craton are sparse, there is evidence that the region did not exceed greenschist-facies conditions. For instance, the Challenger gold deposit in the central Christie Domain records fluid-induced greenschist-facies retrograde metamorphism of granulite-facies Sleafordian protoliths, with temperatures thought not to have exceeded ~ 350 °C (Tomkins et al. 2004). However, at Mount Christie near Skuse Hill and Aristarchus, the Kimban Orogeny is interpreted to have been characterised by higher temperatures (~ 600–700 °C) as indicated by garnet-breakdown reactions and retrograde biotite-sillimanite-quartz assemblages after cordierite and K-feldspar (Daly and Fanning 1993). However, the retrograde assemblages in the metasedimentary rocks have more recently been interpreted to have developed as a consequence of c. 2430–2300 Ma slow cooling following Sleafordian granulite-facies metamorphism (Halpin and Reid 2016). The wide range of temperatures recorded by amphibole from the different mafic intrusions in this study (Fig. 4) suggests a proportion of these may not necessarily be representative of the maximum temperatures reached during the Kimban Orogeny in the central Gawler Craton. However, the temperature data can be used in support of the interpretations from apatite-amphibole textural relationships (Figs. 3, S1−S4) and apatite REE data (Fig. 9), both of which are important in better elucidating the mechanism for apatite Lu–Hf re-equilibration (i.e., thermally activated volume diffusion or recrystallisation).

Skuse Hill region (samples 3825238, 3825268, 3825272)

Kimban-aged apatite in sample 3825268 from Skuse Hill drillhole BLACKFELLOW HILL 1 (c. 1711 Ma; Fig. 8C) shows micro-voids (indicative of partial dissolution; Fig. S4; Harlov 2015) and fine-grained biotite occurs at the apatite margins (Figs. 3F, S3). Both observations are consistent with metamorphic and/or metasomatic recrystallisation. Despite this, apatite LREE compositions appear intact, plotting in the ultramafic field on the Sr/Y versus ∑LREE discrimination plot (Fig. 9C), and chondrite-normalised Sm/Ce ratios are below 1 (0.1–0.6; supplementary material 8), owing to MREE depletion relative to the LREEs (Fig. 10). One possibility is that the fluid that facilitated apatite recrystallisation

was mafic–ultramafic in character and therefore potentially locally generated. Another possibility is that dissolution-reprecipitation and the development of partial dissolution textures in apatite (e.g., Harlov et al. 2005) proceeded effectively as a closed chemical system, whereby the comparatively compatible LREEs negligibly changed their abundances, but the Lu–Hf system was reset during regrowth. The latter interpretation is supported by the absence of LREE-bearing accessory minerals such as allanite, epidote, and monazite, which would conceivably modify the trace-element abundances in apatite from sample 3825268 (e.g., Harlov 2015; Henrichs et al. 2018; O'Sullivan et al. 2020). Apatite in sample 3825268 is texturally associated with the colourless amphiboles, cummingtonite and tremolite (amp^2, amp^3; Fig. 3E, F). While the Ti-in-amphibole thermometer could not be applied to cummingtonite due to insufficient Ti and Ca, tremolite records equilibration temperatures between 368 and 406 °C (Figs. 4, 10, S3; supplementary material 2), supporting a dissolution-reprecipitation driver for Lu–Hf isotopic resetting in apatite.

Apatite in sample 3825272 from the same drillhole is overprinted by allanite (Fig. 3H) and has highly dispersed LREEs (Sm/Ce = 0.6–4.0; Figs. 9D, 10). Therefore, the interpreted Lu–Hf apparent date of 1857 ± 82 Ma (MSWD = 3.81) likely reflects partial (near-complete) recrystallisation, possibly as a consequence of the 1730–1690 Ma Kimban Orogeny. Omission of the two oldest analyses (Fig. 8D) produces a younger and more precise $^{176}Hf/^{176}Lu$ weighted mean age of 1806 ± 54 Ma (MSWD = 1.27), which is within uncertainty of the Kimban Lu–Hf ages from other Skuse Hill samples (Fig. 8B, C). Apatite occurs between plagioclase grains and is associated with magnesio-ferri-hornblende intergrown with quartz (Figs. 3G, S3), with the amphibole recording Ti thermometry temperatures between 508 and 570 °C (Fig. 4; supplementary material 2). These temperatures are insufficient to promote Hf thermal volume diffusion in apatite (e.g., Glorie et al. 2023), which supports a metasomatic driver for Lu–Hf isotopic modification.

Apatite in sample 3825236 from nearby drillhole SKUSE HILL 2 (Lu–Hf age of c. 1735 Ma, U–Pb age of c. 1689 Ma; Figs. 7B, 8B) has dispersed LREE concentrations (Sm/Ce = 1.3–3.6; Figs. 9B, 10) and partial dissolution textures (Fig. 3D), with extremely fine-grained amphibole occurring at the apatite margins (Fig. S4). These results, together with the observation that the sample is proximal to samples 3825268 and 3825272 which contain recrystallised apatite, suggest that recrystallisation also drove Lu–Hf re-equilibration in apatite from sample 3825236.

Aristarchus prospect (samples 3848685, 3848686)

Samples 3848685 and 3848686 from Aristarchus drillhole DMDD-001 are separated by ~ 20 m and so the data from these samples is therefore considered together. Sample 3848686 contains Kimban-aged apatite (1632 ± 47 Ma within uncertainty of c. 1690–1670 Ma Tunkillia Suite; Fig. 8G) with dispersed LREE signatures possibly indicative of recrystallisation (Sm/Ce = 0.2–3.7; Figs. 9G, 10). The c. 1590 Ma U–Pb age recorded by apatite (Fig. 7G) reflects complete Pb resetting coinciding with Hiltaba-related processes. Apatite is associated with magnesio-ferri-hornblende which records temperatures below those expected to promote Lu–Hf thermal re-equilibration (514–530 °C; Figs. 3N, 4; supplementary material 2), thereby supporting the interpretation of recrystallisation. While apatite in sample 3848685 from the same drillhole gives a similar Hiltaba U–Pb age (c. 1595 Ma; Fig. 7F), a similar Kimban Lu–Hf age (c. 1666 Ma; Fig. 8F), and similarly highly dispersed LREE signatures (Sm/Ce = 0.3–7.0; Figs. 9F, 10), the two amphiboles in the sample, pargasite (amp^1) and magnesio-hornblende (amp^2), record comparatively high temperatures between 707–732 °C and 768–795 °C, respectively (Fig. 4; supplementary material 2). These temperatures are more consistent with the earlier Sleafordian Orogeny in the Aristarchus-Mt Christie region (Halpin and Reid 2016) and probably do not relate to apatite recrystallisation during the Kimban, especially given the lower temperatures recorded by amphibole in more severely retrogressed sample 3848686. This interpretation implies sample 3848685 did not witness the comparatively low temperature amphibole overprint which presumably completely obliterated relict higher temperature amphibole in sample 3848686. Despite the absence of this overprint in sample 3848685, the available evidence suggests Kimban-aged metasomatism facilitated apatite recrystallisation, given the presence of partial dissolution features in apatite (Fig. 3M) and the pattern of highly dispersed LREE signatures (Fig. 9F).

South-west of Tarcoola goldfield (sample 3848707)

Sample 3848707 located ~ 100 km south-east of the Aristarchus-Skuse Hill region in drillhole BGDDH 4 also contains Kimban-aged apatite (c. 1748 Ma; Fig. 8H) and highly dispersed LREE patterns consistent with the presence of epidote and monazite in the sample (Sm/Ce = 0.5–5.5; Figs. 9H, 10). These features provide evidence that the re-equilibrated Lu–Hf age is the result of recrystallisation and/or metasomatism. Interestingly, sample 3848707 contains pargasitic amphibole which records relatively high temperatures (749–779 °C; Fig. 4; supplementary material 2). It is not clear petrographically if apatite is in textural equilibrium with high-temperature pargasite, and with no evidence of a lower temperature amphibole overprint in the sample, this leaves open the possibility that pargasite formed during the Kimban Orogeny and the apatite Lu–Hf age resulted from a mechanism of Hf thermal volume diffusion as opposed to

recrystallisation. If the pargasitic amphibole developed during the Sleafordian Orogeny, however, apatite in the sample may have formed through recrystallisation.

Muckanippie region and far north-west Christie Domain (samples 3479680, 3825255)

Without zircon U–Pb data from outcrop sample 3479680 from the Muckanippie region, it is difficult to establish whether the apatite Lu–Hf age is primary or secondary (c. 1732 Ma; Fig. 8A). If the apatite is secondary and the age of the mafic intrusion is between c. 2479–2467 Ma, the textural evidence for partial dissolution (Fig. 3C) points to recrystallisation as the mechanism for Lu–Hf resetting in apatite. Supporting this interpretation is that apatite is in textural equilibrium with blue-green magnesio-hastingsite (amp^2; Figs. 3B, S3) which overprints magnesio-ferri-hornblende (amp^1) and records temperatures between 537 and 593 °C (Fig. 4; supplementary material 2). These temperatures are likely too low to facilitate Hf diffusion in apatite. In an alternative scenario, the intrusion could have been emplaced during the c. 1730–1690 Ma Kimban Orogeny, which is supported by ostensibly unmodified near-flat light- to mid-REE signatures in apatite (Sm/Ce = 0.5–0.7; Figs. 9A, 10), and TMI imagery which suggests the Muckanippie Suite intrudes the Mulgathing Complex.

Notably, anorthosite sample 3479680 is undeformed, as is also the case for sample 3825255 from the far north-west Christie Domain near the Karari Shear Zone. The latter is interpreted to have been emplaced in the early Palaeoproterozoic despite the absence of zircon data. While the apatite Lu–Hf age from sample 3825255 (c. 2158 Ma) is not interpreted as primary because of the dispersion in the data, the relatively high MSWD, and it does not correlate with regional tectonism (Fig. 8E), it is significantly older than the dominantly Kimban apatite Lu–Hf ages recorded by the Aristarchus, Skuse Hill region, and south-west Tarcoola samples (Fig. 10), which all preserve evidence for deformation (Figs. S1, S2; Table 1). As well as the older Lu–Hf age, apatite in sample 3825255 appears relatively pristine, with grains lacking micro-voids and pervasive fractures–features of which usually characterise recrystallised apatite (Fig. S4). Additionally, LREE concentrations in apatite appear to be relatively unmodified compared to most other samples in the study (Fig. 9E) and the vast majority of Sm/Ce values are below 1 (0.4–2.0; median = 0.7; Fig. 10). Although the occurrence of recrystallised apatite in the sample cannot be ruled out, the above textural and compositional evidence does not support such a mechanism for the facilitation of Lu–Hf resetting in apatite. Sample 3825255 contains two textural generations of magnesio-ferri-hornblende, with the comparatively coarse-grained generation in textural equilibrium with relict orthopyroxene (amp^1; Fig. S2) and the fine-grained generation clearly overprinting relict orthopyroxene (amp^2; Figs. 3J, S2, S3). Each generation records Ti thermometry temperatures between 777 and 819 °C and 689–782 °C, respectively (Fig. 4; supplementary material 2), which are sufficient to promote Hf thermal volume diffusion in apatite (e.g., Barfod et al. 2005; Glorie et al. 2023). If texturally late hornblende (amp^2) is younger than the Sleafordian Orogeny and potentially Kimban-aged (given the apatite U–Pb age of c. 1713 Ma; Fig. 8E), it is possible the interpreted apparent apatite Lu–Hf age of c. 2158 Ma is a consequence of partial thermal resetting.

Possible controls on Lu–Hf re-equilibration

The samples from Aristarchus and Skuse Hill containing interpreted recrystallised apatite come from the central-southern Christie Domain region, which appears not to have witnessed significant Kimban-aged thermal reworking. The most proximal Kimban-aged granites are located in the northern Fowler Domain (Fanning et al. 2007; Reid 2015) and western Wilgena Domain (Brown et al. 2022), some ~ 15–30 km from Aristarchus and Skuse Hill. In contrast, samples 3825255 and 3848707, which potentially contain apatite with variably thermally modified Lu–Hf signatures, are proximal to regions of the Gawler Craton that have witnessed comparatively extensive Kimban- and post-Kimban-aged tectonism (Figs. 1, 2). Sample 3825255 is from the far north-west Christie Domain, and although this region is inferred to have witnessed temperatures of only ~ 300 °C during the Palaeoproterozoic (Fraser et al. 2012), the sample is sourced from a drillhole proximal to the Karari Shear Zone (Fig. 2), which separates the Christie and Nawa domains (Fig. 2), and was activated during the Kimban Orogeny and emplacement of the Tunkillia Suite. Pressure–temperature conditions for the Nawa Domain at this time are inferred to have reached at least lower granulite-facies given the pervasive occurrence of monazite and zircon (Fraser et al. 2012). Furthermore, magnetite-bearing metasedimentary rocks in the south-west Nawa Domain proximal to the Karari Shear Zone were metamorphosed to ultrahigh-temperatures during the Kimban Orogeny (Cutts et al. 2013). Sample 3848707 is from a drillhole in the vicinity of the Finke Shear Zone and southern extension of the Tarcoola Fault at the boundary of the Wilgena and Harris Greenstone domains (Fig. 2). The area preserves an extensive record of felsic to intermediate granitoid emplacement during the Kimban Orogeny (Budd 2006; Bockmann et al. 2019) and during subsequent magmatism from c. 1620–1590 Ma (Budd 2006; Bockmann et al. 2019; Brown et al. 2022).

The relationship between the mechanism of apatite Lu–Hf re-equilibration (i.e., recrystallisation vs thermal volume diffusion) and regional setting described above is perhaps unsurprising, however, it is interesting to speculate on the

possible smaller scale controls on Lu–Hf re-equilibration in apatite. Evidently, metasomatism is the fundamental driver of apatite dissolution-reprecipitation (e.g., Harlov et al. 2005; Harlov 2015) and, as with the apatite U–Pb system (e.g., Kirkland et al. 2018; and references therein), the Lu–Hf system in apatite is particularly susceptible to such processes–as demonstrated in this study. A multitude of studies have also explored the influence of strain on the U–Pb system in apatite (e.g., Odlum and Stockli 2020; Prent et al. 2020; Ribeiro et al. 2020; Odlum et al. 2022), however, similar investigations in the context of the Lu–Hf system in apatite are lacking. In this study, regardless of the driver of apatite partial isotopic resetting in sample 3825255, it is interesting to observe that it is the least deformed sample (e.g., texturally granoblastic and preserves no evidence of deformation in plagioclase) and records an apatite Lu–Hf age that best approximates the age of early Palaeoproterozoic mafic magmatism (Fig. 10). Although this potential relationship has not yet been explored in the context of mafic intrusions, a clear relationship between the extent of Lu–Hf isotopic resetting and the degree of deformation has recently been documented in various granitoids from across Australia, with apatite in comparatively deformed granitoids recording younger, re-equilibrated Lu–Hf ages (Glorie et al. 2023).

Conclusions

The investigated polymetamorphic mafic intrusions from the central-western Gawler Craton were emplaced pre- to syn-Sleafordian Orogeny between c. 2479 Ma and c. 2467 Ma. A post-Sleafordian (c. 2475–2410 Ma) amphibole-dominant hydrous overprint on the primary magmatic assemblages was hypothesised based on textural evidence. Apatite laser-ablation Lu–Hf and U–Pb geochronology was undertaken to test this hypothesis, with both isotopic systems recording significantly younger ages correlating with the c. 1730–1690 Ma Kimban Orogeny and the c. 1590–1575 Ma Hiltaba magmatic event, respectively. Based principally on textural and compositional evidence, the apatite U–Pb ages are attributed to thermal re-equilibration and the older Lu–Hf ages are interpreted to reflect re-equilibration facilitated primarily by dissolution-reprecipitation, but also thermally activated volume diffusion. At low to moderate temperatures, mafic-hosted apatite is susceptible to complete recrystallisation in rocks that have weak to moderate foliations (e.g., Aristarchus, Skuse Hill), which underscores the importance of detailed petrological investigations when interpreting geochronological data. At higher temperatures in the absence of strain, the evidence suggests that the Lu–Hf system in apatite is comparatively robust, with the example of granoblastic sample 3825255 near the Karari Shear Zone, which records an interpreted partially reset Lu–Hf apatite age.

The observations and interpretations outlined in this study advance our understanding of the complex role that both metamorphism and deformation play on the ability of apatite hosted in mafic intrusive rocks to retain primary Lu–Hf isotopic signatures. While we do not attempt to precisely evaluate which of these drivers (thermal or strain-related) are more efficient in inducing Lu–Hf re-equilibration, we demonstrate that in a dynamic polymetamorphic system spanning the Neoarchean to early Mesoproterozoic, the apatite Lu–Hf system responds variably to such drivers.

Supplementary Information The online version contains supplementary material available at https://doi.org/10.1007/s00410-024-02117-0.

Acknowledgements Adelaide Microscopy staff Sarah Gilbert, Aoife McFadden, and Ben Wade are thanked for providing assistance with LA–ICP–MS, SEM, and EPMA procedures, respectively. Curtin University staff Allen Kennedy and Hao Gao are thanked for providing assistance with SHRIMP procedures. Jess Bonsell is thanked for drafting figures of the regional geology. The manuscript benefited greatly from detailed reviews by Jeffrey Oalmann and David Chew. Daniela Rubatto and Dante Canil are thanked for editorial handling of the manuscript. Published with permission of the Director, Geological Survey of South Australia, Department for Energy and Mining.

Author contributions Study design (DB, AR, MW), fieldwork (AR, MP), sample preparation and data acquisition, (DB, AR, EJ, MW, AS, MP, CK, CW, AVL), data analysis and interpretation (all authors). DB prepared the manuscript with contributions from all co-authors.

Funding This work was financially supported by the Geological Survey of South Australia, Department for Energy and Mining.

Data availability Data are included in the supplementary material.

Declarations

Conflict of interest The authors have no competing interests to declare that are relevant to the content of this article.

References

Barfod GH, Krogstad EJ, Frei R, Albarède F (2005) Lu-Hf and PbSL geochronology of apatites from Proterozoic terranes: a first look at Lu-Hf isotopic closure in metamorphic apatite. Geochim Cosmochim Acta 69(7):1847–1859. https://doi.org/10.1016/j.gca.2004.09.014

Bockmann MJ, Wilson TC, Pawley MJ, Payne JL, Dutch RA (2019) LA–ICP–MS geochronology from the Tarcoola goldfield region 2018–2019. Report book 2019/00015. Department for Energy and Mining, Adelaide, South Australia

Brown D, Pawley M, Williams M, Reid A, Jagodzinski E (2022) Zircon LA–ICP–MS geochronological and geochemical results from the central-western Gawler craton. Report book 2022/00008. Department for Energy and Mining, Adelaide, South Australia

Budd A (2006) The Tarcoola goldfield of the central Gawler gold province, and the Hiltaba association granites, Gawler craton. PhD thesis, Australian National University, South Australia

Cave B, Lilly R, Simpson A, McGee L (2023) A revised model for the George Fisher and Hilton Zn-Pb-Ag deposits, NW Queensland: insights from the geology, age and alteration of the local dolerite dykes. Ore Geol Rev 154:105311. https://doi.org/10.1016/j.oregeorev.2023.105311

Cherniak DJ (2000) Rare earth element diffusion in apatite. Geochim Cosmochim Acta 64(22):3871–3885. https://doi.org/10.1016/S0016-7037(00)00467-1

Chew DM, Spikings RA (2015) Geochronology and thermochronology using apatite: time and temperature. Lower Crust Surf Elem 11(3):189–194. https://doi.org/10.2113/gselements.11.3.189

Chew DM, Sylvester PJ, Tubrett MN (2011) U-Pb and Th–Pb dating of apatite by LA-ICPMS. Chem Geol 280(1):200–216. https://doi.org/10.1016/j.chemgeo.2010.11.010

Cochrane R, Spikings RA, Chew D, Wotzlaw J-F, Chiaradia M, Tyrrell S, Schaltegger U, Van der Lelij R (2014) High temperature (>350°C) thermochronology and mechanisms of Pb loss in apatite. Geochim Cosmochim Acta 127:39–56. https://doi.org/10.1016/j.gca.2013.11.028

Cutts KA, Kelsey DE, Hand M (2013) Evidence for late Paleoproterozoic (ca 1690–1665Ma) high- to ultrahigh-temperature metamorphism in southern Australia: Implications for Proterozoic supercontinent models. Gondwana Res 23(2):617–640. https://doi.org/10.1016/j.gr.2012.04.009

Dai L-Q, Zhao Z-F, Zheng Y-F, Li Q, Yang Y, Dai M (2011) Zircon Hf–O isotope evidence for crust–mantle interaction during continental deep subduction. Earth Planet Sci Lett 308(1):229–244. https://doi.org/10.1016/j.epsl.2011.06.001

Daly SJ, Fanning CM (1993) Archaean. In: Drexel JF, Preiss WV, Parker AJ (eds) The geology of South Australia; Vol 1, The Precambrian, geological survey of South Australia. Bulletin 54, Adelaide, South Australia, Australia, pp 32–49

De Bievre P, Taylor PDP (1993) Table of the isotopic compositions of the elements. Int J Mass Spectrom Ion Process 123(2):149–166. https://doi.org/10.1016/0168-1176(93)87009-h

Direen NG, Cadd AG, Lyons P, Teasdale JP (2005) Architecture of Proterozoic shear zones in the Christie domain, western Gawler craton, Australia: geophysical appraisal of a poorly exposed orogenic terrane. Precambr Res 142:28–44

Dutch RA, Hand M, Kelsey DE (2010) Unravelling the tectonothermal evolution of reworked archean granulite facies metapelites using in situ geochronology: an example from the Gawler craton. Aust J Metamorph Geol 28(3):293–316. https://doi.org/10.1111/j.1525-1314.2010.00867.x

Fanning CM, Reid AJ, Teale G (2007) A geochronological framework for the Gawler craton. South Australia Geological Survey, South Australia. Bulletin 55

Ferris G, Schwarz MP (2004) Definition of the tunkillia suite, western Gawler craton. Miner Energy South Aust J 34:32–41

Fisher CM, Vervoort JD (2018) Using the magmatic record to constrain the growth of continental crust—the eoarchean zircon Hf record of greenland. Earth Planet Sci Lett 488:79–91. https://doi.org/10.1016/j.epsl.2018.01.031

Fraser G, Reid A, Stern R (2012) Timing of deformation and exhumation across the Karari shear zone, north-western Gawler craton, South Australia. Aust J Earth Sci 59(4):547–570. https://doi.org/10.1080/08120099.2012.678586

Gillespie J, Glorie S, Khudoley A, Collins AS (2018) Detrital apatite U-Pb and trace element analysis as a provenance tool: insights from the Yenisey Ridge (Siberia). Lithos. https://doi.org/10.1016/j.lithos.2018.05.026

Gillespie J, Kirkland CL, Kinny PD, Simpson A, Glorie S, Rankenburg K (2022) Lu–Hf, Sm–Nd, and U-Pb isotopic coupling and decoupling in apatite. Geochim Cosmochim Acta. https://doi.org/10.1016/j.gca.2022.09.038

Glorie S, Jepson G, Konopelko D, Mirkamalov R, Meeuws F, Gilbert S, Gillespie J, Collins AS, Xiao W, Dewaele S, De Grave J (2019) Thermochronological and geochemical footprints of post-orogenic fluid alteration recorded in apatite: implications for mineralisation in the uzbek tian shan. Gondwana Res 71:1–15. https://doi.org/10.1016/j.gr.2019.01.011

Glorie S, Gillespie J, Simpson A, Gilbert S, Khudoley A, Priyatkina N, Hand M, Kirkland Christopher L (2022) Detrital apatite Lu–Hf and U-Pb geochronology applied to the southwestern Siberian margin. Terra Nova 34(3):201–209. https://doi.org/10.1111/ter.12580

Glorie S, Hand M, Mulder J, Simpson A, Emo Robert B, Kamber B, Fernie N, Nixon A, Gilbert S (2023) Robust laser ablation Lu-Hf dating of apatite: an empirical evaluation. Geol Soc Lond Spec Publ. https://doi.org/10.1144/SP537-2022-205

Hall JW, Glorie S, Reid AJ, Boone SC, Collins AS, Gleadow A (2018) An apatite U-Pb thermal history map for the northern Gawler Craton. S Aust Geosci Front 9(5):1293–1308. https://doi.org/10.1016/j.gsf.2017.12.010

Halpin JA, Reid AJ (2016) Earliest Paleoproterozoic high-grade metamorphism and orogenesis in the Gawler craton, South Australia: the southern cousin in the rae family? Precambr Res 276:123–144. https://doi.org/10.1016/j.precamres.2016.02.001

Hand M, Reid A, Jagodzinski E (2007) Tectonic framework and evolution of the Gawler craton, South Australia. Econ Geol 102:1377–1395

Hand M, Reid AJ, Dutch R, Lane K, Jagodzinski EA (2012) Transpression and lower crustal extrusion: a transect across the Paleoproterozoic kalinjala shear system in the southeastern Gawler craton. Report book 2012/00017. Department for Manufacturing, Innovation, Trade, Resources and Energy, Adelaide, South Australia

Harlov DE (2015) Apatite: a fingerprint for metasomatic processes. Elements 11(3):171–176. https://doi.org/10.2113/gselements.11.3.171

Harlov DE, Wirth R, Förster H-J (2005) An experimental study of dissolution–reprecipitation in fluorapatite: fluid infiltration and the formation of monazite. Contrib Miner Petrol 150(3):268–286. https://doi.org/10.1007/s00410-005-0017-8

Hawthorne FC, Oberti R, Harlow GE, Maresch WV, Martin RF, Schumacher JC, Welch MD (2012) Nomenclature of the amphibole supergroup. Am Miner 97(11–12):2031–2048. https://doi.org/10.2138/am.2012.4276

Henrichs IA, O'Sullivan G, Chew DM, Mark C, Babechuk MG, McKenna C, Emo R (2018) The trace element and U-Pb systematics of metamorphic apatite. Chem Geol 483:218–238. https://doi.org/10.1016/j.chemgeo.2017.12.031

Hoatson DM, Sun S-S, Duggan MB, Davies MB, Daly SJ, Purvis AC (2005) Late Archaean Lake Harris komatiite, central Gawler craton, South Australia: geologic setting and geochemistry. Econ Geol 100:349–374

Jagodzinski EA, Reid AJ (2017) PACE geochronology: results of collaborative geochronology projects, 2013–2015. Government of South Australia. Department of the Premier and Cabinet. Report book, 2015/00003

Jagodzinski EA, Black L, Frew RA, Foudoulis C, Reid A, Payne J, Zang W, Schwarz MP (2006) Compilation of SHRIMP U-Pb geochronological data for the Gawler craton, South Australia 2005–2006. Primary Industries and Resources South Australia Report book 2006/20

Jagodzinski E, Reid A, Fraser G (2009) Compilation of SHRIMP U-Pb geochronological data for the mulgathing complex, Gawler craton, South Australia, 2007–2009. South Australia. Department of Primary Industries and Resources. Report book 2009/16

Jochum KP, Weis U, Stoll B, Kuzmin D, Yang Q, Raczek I, Jacob DE, Stracke A, Birbaum K, Frick DA, Günther D, Enzweiler J (2011) Determination of reference values for NIST SRM 610–617 glasses

following ISO guidelines. Geostand Geoanal Res 35(4):397–429. https://doi.org/10.1111/j.1751-908X.2011.00120.x

Kharkongor M, Glorie S, Mulder J, Kirkland Christopher L, Chew D, Kohn B, Simpson A (2023) Apatite laser ablation LuHf geochronology: a new tool to date mafic rocks. Chem Geol. https://doi.org/10.1016/j.chemgeo.2023.121630

Kirkland CL, Hollis J, Danišík M, Petersen J, Evans NJ, McDonald BJ (2017) Apatite and titanite from the Karrat Group, Greenland; implications for charting the thermal evolution of crust from the U-Pb geochronology of common Pb bearing phases. Precambr Res 300:107–120. https://doi.org/10.1016/j.precamres.2017.07.033

Kirkland CL, Yakymchuk C, Szilas K, Evans N, Hollis J, McDonald B, Gardiner NJ (2018) Apatite: a U-Pb thermochronometer or geochronometer? Lithos 318–319:143–157. https://doi.org/10.1016/j.lithos.2018.08.007

Li Y, Vermeesch P (2021) Short communication: Inverse isochron regression for Re–Os. K-Ca Other Chronom Geochronol 3(2):415–420. https://doi.org/10.5194/gchron-3-415-2021

Liao Y, Wei C, Rehman HU (2021) Titanium in calcium amphibole: behavior and thermometry. Am Miner 106(2):180–191. https://doi.org/10.2138/am-2020-7409

Ludwig KR (2009) SQUID 2.50: A user's manual. Berkeley Geochronology Center Special Publication No. 5., Berkeley California, USA

McFarlane CRM (2006) Palaeoproterozoic evolution of the challenger Au deposit, South Australia, from monazite geochronology. J Metamorph Geol 24:75–87

McFarlane CRM, Mavrogenes JA, Tomkins AG (2007) Recognizing hydrothermal alteration through a granulite facies metamorphic overprint at the challenger Au deposit, South Australia. Chem Geol 243:64–89

Nebel O, Morel MLA, Vroon PZ (2009) Isotope dilution determinations of Lu, Hf, Zr, Ta and W, and Hf isotope compositions of NIST SRM 610 and 612 glass wafers. Geostand Geoanal Res 33(4):487–499. https://doi.org/10.1111/j.1751-908X.2009.00032.x

Nixon AL, Glorie S, Collins AS, Blades ML, Simpson A, Whelan JA (2022) Inter-cratonic geochronological and geochemical correlations of the Derim Derim–Galiwinku/Yanliao reconstructed large igneous province across the North Australian and North China cratons. Gondwana Res 103:473–486. https://doi.org/10.1016/j.gr.2021.10.027

Norris A, Danyushevsky L (2018) Towards estimating the complete uncertainty budget of quantified results measured by LA-ICP-MS. In: Goldschmidt, Boston

Odlum ML, Stockli DF (2020) Geochronologic constraints on deformation and metasomatism along an exhumed mylonitic shear zone using apatite U-Pb, geochemistry, and microtextural analysis. Earth Planet Sci Lett 538:116177. https://doi.org/10.1016/j.epsl.2020.116177

Odlum ML, Levy DA, Stockli DF, Stockli LD, DesOrmeau JW (2022) Deformation and metasomatism recorded by single-grain apatite petrochronology. Geology 50(6):697–703. https://doi.org/10.1130/g49809.1

Orejana D, Villaseca C, Kristoffersen M (2020) Geochemistry and geochronology of mafic rocks from the Spanish Central System: constraints on the mantle evolution beneath central Spain. Geosci Front 11(5):1651–1667. https://doi.org/10.1016/j.gsf.2020.01.002

O'Sullivan G, Chew D, Kenny G, Henrichs I, Mulligan D (2020) The trace element composition of apatite and its application to detrital provenance studies. Earth Sci Rev 201:103044. https://doi.org/10.1016/j.earscirev.2019.103044

Parker AJ (1993) Kimban Orogeny. In: Drexel JF, Preiss WV, Parker AJ (eds) The geology of South Australia, vol 1. The Precambrian. Geological Survey of South Australia, Adelaide, South Australia, pp 71–82

Payne JL, Ferris G, Barovich KM, Hand M (2010) Pitfalls of classifying ancient magmatic suites with tectonic discrimination diagrams: an example from the Paleoproterozoic tunkillia suite, southern Australia. Precambr Res 177:227–240

Pochon A, Poujol M, Gloaguen E, Branquet Y, Cagnard F, Gumiaux C, Gapais D (2016) U-Pb LA-ICP-MS dating of apatite in mafic rocks: Evidence for a major magmatic event at the Devonian-Carboniferous boundary in the Armorican Massif (France). Am Mineral 101(11):2430–2442. https://doi.org/10.2138/am-2016-5736

Prent AM, Beinlich A, Raimondo T, Kirkland CL, Evans NJ, Putnis A (2020) Apatite and monazite: an effective duo to unravel superimposed fluid-flow and deformation events in reactivated shear zones. Lithos 376–377:105752. https://doi.org/10.1016/j.lithos.2020.105752

Reid AJ (2015) Zircon U-Pb geochronology from selected Paleoproterozoic igneous rocks of the Gawler craton by laser ablation-inductively coupled plasma mass spectrometry. Department of State Development. Report book, 2015/00025

Reid AJ, Hand M (2012) Mesoarchean to Mesoproterozoic evolution of the southern Gawler Craton, South Australia. Episodes 35:216–225

Reid AJ, Jagodzinski EA, Fraser GL, Pawley MJ (2014) SHRIMP U-Pb zircon age constraints on the tectonics of the Neoarchean to early Paleoproterozoic transition within the mulgathing complex, Gawler craton South Australia. Precambr Res 250:27–49. https://doi.org/10.1016/j.precamres.2014.05.013

Reid AJ, Tiddy CJ, Jagodzinski EA, Crowley JL, Conor CCH, Brotodewo A, Wade CE (2021) Precise zircon U-Pb geochronology of Hiltaba suite granites, Point Riley, Yorke Peninsula. Department for Energy and Mining. Report book, 2021/00001

Ribeiro BV, Lagoeiro L, Faleiros FM, Hunter NJR, Queiroga G, Raveggi M, Cawood PA, Finch M, Campanha GAC (2020) Strain localization and fluid-assisted deformation in apatite and its influence on trace elements and U-Pb systematics. Earth Planet Sci Lett 545:116421. https://doi.org/10.1016/j.epsl.2020.116421

Sambridge MS, Compston W (1994) Mixture modelling of multi-component data sets with application to ion-probe zircon ages. Earth Planet Sci Lett 128:373–390

Schoene B, Bowring SA (2006) U-Pb systematics of the McClure Mountain syenite: thermochronological constraints on the age of the 40Ar/39Ar standard MMhb. Contrib Miner Petrol 151(5):615. https://doi.org/10.1007/s00410-006-0077-4

Schoene B, Bowring SA (2007) Determining accurate temperature–time paths from U-Pb thermochronology: an example from the Kaapvaal craton, southern Africa. Geochim Cosmochim Acta 71(1):165–185. https://doi.org/10.1016/j.gca.2006.08.029

Simpson A, Gilbert S, Tamblyn R, Hand M, Spandler C, Gillespie J, Nixon A, Glorie S (2021) In-situ Lu Hf geochronology of garnet, apatite and xenotime by LA ICP MS/MS. Chem Geol. https://doi.org/10.1016/j.chemgeo.2021.120299

Simpson A, Glorie S, Hand M, Spandler C, Gilbert S, Cave B (2022) In situ Lu–Hf geochronology of calcite. Geochronology 4(1):353–372. https://doi.org/10.5194/gchron-4-353-2022

Stern RA, Bodorkos S, Kamo SL, Hickman AH, Corfu F (2009) Measurement of SIMS instrumental mass fractionation of Pb isotopes during zircon dating. Geostand Geoanal Res 33(2):145–168. https://doi.org/10.1111/j.1751-908X.2009.00023.x

Sun SS, McDonough WF (1989) Chemical and isotopic systematics of oceanic basalts; implications for mantle composition and processes. In: Saunders AD, Norry MJ (eds) Magmatism in the ocean basins, vol 42. Geological Society London, London, pp 313–345

Swain G, Woodhouse A, Hand M, Barovich K, Schwarz M, Fanning CM (2005) Provenance and tectonic development of the late

Archaean Gawler Craton, Australia; U-Pb zircon, geochemical and Sm-Nd isotopic implications. Precambr Res 141:106–136

Thomson SN, Gehrels GE, Ruiz J, Buchwaldt R (2012) Routine low-damage apatite U-Pb dating using laser ablation–multicollector–ICPMS. Geochem Geophys Geosyst. https://doi.org/10.1029/2011GC003928

Thompson J, Meffre S, Maas R, Kamenetsky V, Kamenetsky M, Goemann K, Ehrig K, Danyushevsky L (2016) Matrix effects in Pb/U measurements during LA-ICP-MS analysis of the mineral apatite. J Anal at Spectrom 31(6):1206–1215. https://doi.org/10.1039/C6JA00048G

Tomkins AG, Dunlap WJ, Mavrogenes JA (2004) Geochronological constraints on the Polymetamorphic evolution of the granulite-hosed Challenger gold deposit: implications for assembly of the northwest Gawler craton. Aust J Earth Sci 51:1–14

Vermeesch P (2018) IsoplotR: a free and open toolbox for geochronology. Geosci Front 9(5):1479–1493. https://doi.org/10.1016/j.gsf.2018.04.001

Wade CE, McAvaney SO (2017) Stratigraphy and geochemistry of the 1745–1700 Ma Peter Pan Supersuite. Department of State Development, South Australia. Report book 2016/00026

Wade CE, Payne JL, Barovich KM, Reid AJ, Jagodzinski EA, Curtis S, Hill J (2022) Temporal, geochemical and isotopic constraints on plume-driven felsic and mafic components in a Mesoproterozoic flood rhyolite province. Results Geochem 9:100019. https://doi.org/10.1016/j.ringeo.2022.100019

Whitney DL, Evans BW (2010) Abbreviations for names of rock-forming minerals. Am Miner 95(1):185–187. https://doi.org/10.2138/am.2010.3371

Wiedenbeck M, Allé P, Corfu F, Griffin WL, Meier M, Oberli F, Quadt AV, Roddick JC, Spiegel W (1995) Three natural zircon standards for U-TH-PB, LU-HF, trace element and REE analyses. Geostand Newsl 19(1):1–23

Williams M, Reid AJ (2021) Linking lithostratigraphy to mineral potential for the Archean to earliest Paleoproterozoic mulgathing complex, central Gawler Craton. MESA J 94:4–18